



**HAL**  
open science

## Subsurface Fine-Scale Patterns in an Anticyclonic Eddy Off Cap-Vert Peninsula Observed From Glider Measurements

Nicolas N. Kolodziejczyk, Pierre Testor, Alban Lazar, Vincent Echevin, Gerd Krahmann, Alexis Chaigneau, Claire Gourcuff, Malick Wade, Saliou Faye, Philippe Estrade, et al.

► **To cite this version:**

Nicolas N. Kolodziejczyk, Pierre Testor, Alban Lazar, Vincent Echevin, Gerd Krahmann, et al.. Subsurface Fine-Scale Patterns in an Anticyclonic Eddy Off Cap-Vert Peninsula Observed From Glider Measurements. *Journal of Geophysical Research. Oceans*, 2018, 123 (9), pp.6312-6329. 10.1029/2018JC014135 . hal-02190688

**HAL Id: hal-02190688**

**<https://hal.science/hal-02190688v1>**

Submitted on 25 May 2020

**HAL** is a multi-disciplinary open access archive for the deposit and dissemination of scientific research documents, whether they are published or not. The documents may come from teaching and research institutions in France or abroad, or from public or private research centers.

L'archive ouverte pluridisciplinaire **HAL**, est destinée au dépôt et à la diffusion de documents scientifiques de niveau recherche, publiés ou non, émanant des établissements d'enseignement et de recherche français ou étrangers, des laboratoires publics ou privés.

## RESEARCH ARTICLE

10.1029/2018JC014135

## Subsurface Fine-Scale Patterns in an Anticyclonic Eddy Off Cap-Vert Peninsula Observed From Glider Measurements

## Key Points:

- Anticyclonic near surface eddy is observed from high-resolution gliders measurements in the Eastern Tropical Atlantic
- Fine-scale thermohaline and dissolved oxygen features are observed in the anticyclonic eddy
- This fine-scale feature are likely related to stirring by the mesoscale eddy

## Supporting Information:

- Supporting Information S1

## Correspondence to:

N. Kolodziejczyk,  
nicolas.kolodziejczyk@univ-brest.fr

## Citation:

Kolodziejczyk, N., Testor, P., Lazar, A., Echevin, V., Krahnmann, G., Chaigneau, A., et al. (2018). Subsurface fine-scale patterns in an anticyclonic eddy off Cap-Vert peninsula observed from glider measurements. *Journal of Geophysical Research: Oceans*, 123, 6312–6329. <https://doi.org/10.1029/2018JC014135>

Received 2 MAY 2018

Accepted 11 JUL 2018

Accepted article online 18 JUL 2018

Published online 8 SEP 2018

Nicolas Kolodziejczyk<sup>1,2</sup> , Pierre Testor<sup>1</sup> , Alban Lazar<sup>1</sup>, Vincent Echevin<sup>1</sup>, Gerd Krahnmann<sup>3</sup> , Alexis Chaigneau<sup>4</sup>, Claire Gourcuff<sup>1</sup>, Malick Wade<sup>5</sup>, Saliou Faye<sup>6</sup>, Philippe Estrade<sup>7</sup>, Xavier Capet<sup>1,8</sup>, Laurent Mortier<sup>1</sup>, Patrice Brehmer<sup>8</sup> , Florian Schütte<sup>3</sup>, and Johannes Karstensen<sup>3</sup> 

<sup>1</sup>Sorbonne University (UPMC, Univ Paris 06)-CNRS-IRD-MNHN, LOCEAN Laboratory, Paris, France, <sup>2</sup>University of Brest, CNRS-IRD-Iframer, LOPS Laboratory, IUEM, rue Dumont d'Urville, Plouzané, France, <sup>3</sup>Helmholtz Centre for Ocean Research Kiel (GEOMAR), Kiel, Germany, <sup>4</sup>LEGOS, Université de Toulouse, CNES-CNRS-IRD-UPS, Toulouse, France, <sup>5</sup>Laboratoire des sciences de l'Atmosphère et de l'Océan, Université Gaston Berger, Saint-Louis, Sénégal, <sup>6</sup>Institut Sénégalais de Recherches Agricoles, Centre de Recherche Océanographique de Dakar-Thiaroye, Dakar, Sénégal, <sup>7</sup>IRD, UCAD/LPAOSF, Dakar, Sénégal, <sup>8</sup>Institut de Recherche pour le Développement, Dakar, Sénégal

**Abstract** Glider measurements acquired along four transects between Cap-Vert Peninsula and the Cape Verde archipelago in the eastern tropical North Atlantic during March–April 2014 were used to investigate fine-scale stirring in an anticyclonic eddy. The anticyclone was formed near 12°N off the continental shelf and propagated northwest toward the Cape Verde islands. At depth, between 100 and –400 m, the isolated anticyclone core contained relatively oxygenated, low-salinity South Atlantic Central Water, while the surrounding water masses were saltier and poorly oxygenated. The dynamical and thermohaline subsurface environment favored the generation of fine-scale horizontal and vertical temperature and salinity structures in and around the core of the anticyclone. These features exhibited horizontal scales of O(10–30 km) relatively small with respect to the eddy radius of O(150 km). The vertical scales of O(5–100 m) were associated to density-compensated gradient. Spectra of salinity and oxygen along isopycnals revealed a slope of around  $k^{-2}$  in the 10- to 100-km horizontal scale range. Further analyses suggest that the fine-scale structures are likely related to tracer stirring processes. Such mesoscale anticyclonic eddies and the embedded fine-scale tracers in and around them could play a major role in the transport of South Atlantic Central Water masses and ventilation of the North Atlantic Oxygen Minimum Zone.

## 1. Introduction

The Eastern Tropical North Atlantic (ETNA) holds a nearly stagnant, unventilated, so-called shadow zone (e.g., Luyten et al., 1983; Wyrтки, 1962), which is characterized by old water masses with low dissolved oxygen concentrations (i.e., an oxygen minimum zone [OMZ]) found at shallow and intermediate depths (100–800 m; Brandt et al., 2015; Karstensen et al., 2008). This OMZ, with minimum dissolved oxygen concentration around 40  $\mu\text{mol/kg}$ , is primarily controlled by a sluggish ventilation along the respective isopycnals (Luyten et al., 1983; Wyrтки, 1962) and extends from the eastern boundary into the open ocean, bounded by the more energetic circulation of the subtropical gyre to the north, and the energetic equatorial current regime in the south (Brandt et al., 2015; Karstensen et al., 2008; Luyten et al., 1983). In a larger context, the upper ETNA is characterized by a permanent, large-scale, seasonally varying anticyclonic gyre, the Guinea Gyre (Jiang et al., 2008), associated with the open ocean Dome of Guinea, centered on 10°N–23°W (Siedler et al., 1992; Yamagata & Iisaka, 1995). In the south, the ETNA is bounded by the termination of the North Equatorial Counter Current, and the North Equatorial Current (Stramma et al., 2008) and at the eastern boundary by the Senegal-Mauritanian Upwelling System (SMUS) (Capet et al., 2017). The SMUS, located along the western African coast, is mainly active during boreal winter–spring (January–April; Aristegui et al., 2009; Ndoye et al., 2014). During this season, the intensification of equatorward winds enhances the upwelling of cool, fresh, nutrient-rich and low oxygenated South Atlantic Central Water (SACW), which contrasts with the warmer, saltier, nutrient-depleted and oxygenated offshore waters, namely, the surface tropical water and the subsurface North Atlantic Central Water (NACW).

Ubiquitous surface and subsurface cyclonic and anticyclonic eddies of various origin and nature act as a major transport agent between the coastal waters and the open ocean (e.g., Chelton et al., 2007, 2009;

Alpers et al., 2013; Schütte et al., 2016; Karstensen et al., 2015; Pietri & Karstensen, 2018). They can trap near coastal SACW in their cores and transport the water mass westward to the deep ocean, where it is mixed with the surrounding warmer and saltier NACW (Schütte, Brandt, & Karstensen, 2016). Therefore, the ETNA eddies often exhibit subsurface (within 0- to 500-m depth) thermohaline and dissolved oxygen anomalies (Karstensen et al., 2015; Pietri & Karstensen, 2018; Schütte, Karstensen, et al., 2016; Schütte, Brandt, & Karstensen, 2016). The ETNA eddies are generally characterized by horizontal scales of 50–100 km (Chaigneau et al., 2009), and in spite of the difficulties to consistently track them from satellite observations, their lifetimes are estimated to be between 35 and 200 days (Chelton et al., 2007; Chaigneau et al., 2009). Using altimeter sea level anomaly (SLA), satellite sea surface temperature (SST), and in situ data to derive ETNA eddy statistics, Schütte, Brandt, & Karstensen, 2016, Schütte, Karstensen, et al., 2016 reported the occurrence of three different types of eddies: anticyclonic (AC), cyclonic (CE), and anticyclonic mode water eddies (ACME). ACMEs are particularly efficient in transporting isolated water mass anomalies over large distances of several hundreds to thousands of kilometers (Karstensen et al., 2015; Schütte, Brandt, & Karstensen, 2016). In particular, negative oxygen anomalies were found in both CEs and ACMEs (Karstensen et al., 2015; Karstensen et al., 2017; Schütte, Karstensen, et al., 2016). Averaged over the ETNA region, a reduction of the oxygen concentration by  $\sim 7 \mu\text{mol/kg}$  in the 50- to 100-m depth range could be associated to the enhanced biological consumption along the CE and ACME pathways (Schütte, Karstensen, et al., 2016). Overall, the oxygen loss due to the propagation of oxygen poor waters trapped in CEs and ACMEs may be partly compensated by an oxygen input associated with ACs (Pietri & Karstensen, 2018; Schütte, Karstensen, et al., 2016). Although mode water eddies (ACME) have been studied in some details (Karstensen et al., 2017; Pietri & Karstensen, 2018; Schütte, Brandt, & Karstensen, 2016), studies of normal ACs and associated small-scale features in the ETNA have not been reported.

The role of eddies in ventilation processes of the deep OMZ (between 150- and 600-m depth, Brandt et al., 2015) is not fully understood. The dissolved oxygen supply for the deep OMZ is supposed to be maintained by zonal advection from the oxygenated tropical jets of water masses from subtropical origin, eddy fluxes, local subduction, and mixing (e.g., Tsuchiya et al., 1992; Schott et al., 1995; Schott et al., 1998; Brandt et al., 2010; Banyte et al., 2013; Fischer et al., 2013; Duteil et al., 2014). In particular, the ventilation operated by eddy transport and associated processes of stirring and mixing is not well documented, although eddies are estimated to contribute to 60% of the deep OMZ ventilation (Brandt et al., 2015).

In the ETNA, mesoscale eddies trap and transport westward water mass properties that contrast with the surrounding water masses, dispersing associated gradients and fronts. Temperature, salinity, or dissolved oxygen gradients are stretched and folded several times by mesoscale and submesoscale currents. This process generates smaller spatial scales until the cascade ends at scales where molecular mixing occurs. Various processes leading to tracer filamentation and layering have been reported in the literature. Among them, double diffusion (also known as diffusive convection or salt fingering) creates vertical layers in the tracer field (e.g., May & Kelley, 1997; Ruddick, 1992). Moreover, layering has also been explained by instability and turbulent processes associated with dynamically active tracers such as vorticity (Hua et al., 2013). The stirring of passive tracers in a variety of frontal and eddy regimes has been studied numerically (e.g., Haynes & Anglade, 1997; Klein et al., 1998; Smith & Ferrari, 2009; Meunier et al., 2015), as direct observations of filamentation and layering processes in the ocean are relatively scarce (Cole & Rudnick, 2012; Hua et al., 2013; Ruddick, 1992; Smith & Ferrari, 2009). In the last decades, the development of autonomous observing platforms, such as underwater gliders, has allowed us to observe and study these processes in greater details.

In this study, subsurface thermohaline and dissolved oxygen fine-scale structures observed within an ETNA anticyclonic eddy are characterized for the first time using high-resolution glider observations along a cross-shore transect between Dakar (Senegal) and Cape Verde Archipelago along  $14.7^\circ\text{N}$  (Figure 1). As the minimum horizontal resolution of our glider's measurements reached about 3–5 km, fine-scale filaments ( $O(10\text{--}30 \text{ km})$ ) observed between 100–400 m depth are resolved. Resolving the fine-scale structure of the eddy allows us to analyze the processes that contributed to mixing and stirring of water masses. The article is organized as follows. The data and methods are presented in section 2. The large-scale oceanic context around the AC, the water masses in and around the AC, and the fine-scale filaments observed in and around its core are characterized in section 3. Results are summarized and discussed in section 4.

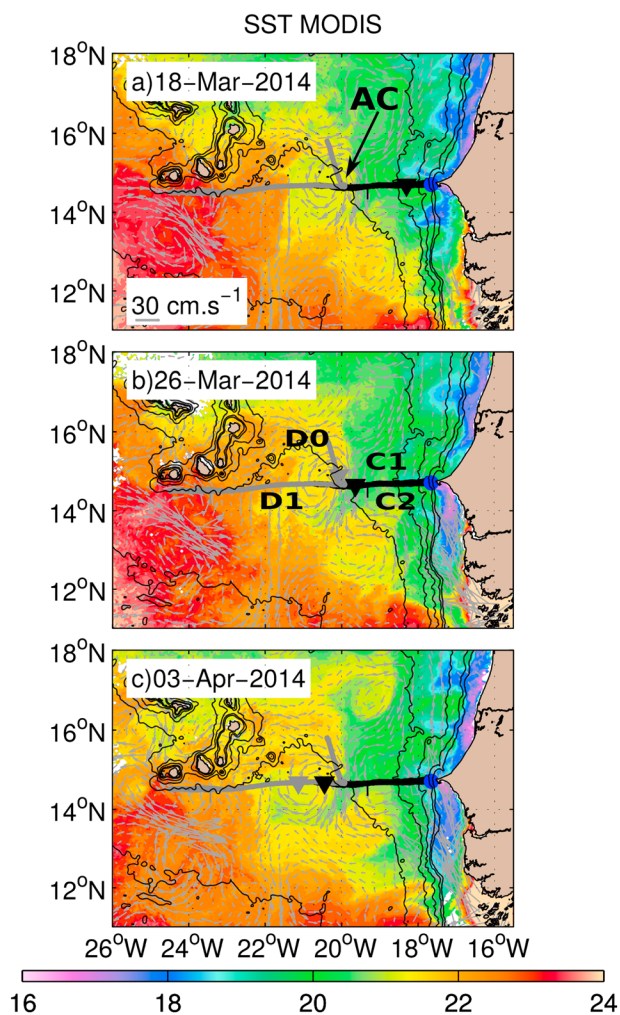


**Figure 1.** MODIS SST (in °C, shading) and AVISO geostrophic surface currents (in cm/s, gray arrows) on (a) 18 March and (b) 26 March, and (c) 3 April 2014. The [−500; −1,000; −2,000; −3,000; −4,000; −5,000] m depth bathymetric contours are also plotted (thin solid black). AC indicates the anticyclone position on Figure 1a. The GLISEN (thick solid black) and DPL21 (thick solid gray) trajectories between March and May 2014, the actual position of GLISEN (black triangle) and DPL21 (gray triangle) gliders at the date indicated in the title of each subfigure are plotted. The blue circle at 14.71°N–17.65°W indicates the position of both the AWA CTD cast used for the salinity offset correction, and the GLISEN deployment. GLISEN = Gliders off Senegal; SST = sea surface temperature; CTD = conductivity-temperature-depth; AWA = Ecosystem Approach to the management of fisheries and the marine environment in West African waters; MODIS = Moderate-resolution Imaging Spectroradiometer.

## 2. Data and Methods

### 2.1. Data

#### 2.1.1. Hydrological Profiles

Gliders were deployed to enhance the observational database in the still poorly sampled ETNA and SMUS off Senegal. The experiment aimed to conduct a detailed survey of the large as well as fine-scale thermohaline and biogeochemical tracer structure along the 14.7°N latitudinal transect between Cap-Vert peninsula (Senegal) and Cape Verde Islands (Figure 1) in order to better document the circulation and water masses structure in this region. Two gliders were deployed: a French glider CAMPE on the deployment *GLISEN* (Gliders off Senegal) off Cap-Vert Peninsula (<http://www.ego-network.org/dokuwiki/doku.php?glider=Campe,GLISEN>) and a second German glider “DEEPLY/IFM02” (hereafter IFM02) on the deployment “DEPL21” (<http://www.ego-network.org/dokuwiki/doku.php?glider=ifm02-deepl21>). Both gliders are so-called deep (i.e., able to dive to 1,000-m depth) G1 Slocum electric gliders (Rudnick et al., 2004; Testor et al., 2010), and both operated between 12 March 2014 and 13 May 2014.

The *GLISEN* glider was deployed off Dakar at 14.7°N–17.65°W on 12 March (Figure 1, blue thick dot). It carried out 412 profiles from the surface to a maximum depth of 1,000 m along four repeated sections. The first (C1; Figure 1) and second (C2; Figure 1) sections extended up to 330 km (20.73°W) off the Cap-Vert peninsula. The third and fourth sections extended only up to 170 km (19.19°W) off Cap-Vert peninsula and were not analyzed in this study. As only the descending profiles of *GLISEN* were recorded, the spatial resolution of the *GLISEN* glider profiles is around  $3.4 \pm 0.8$  km westward of 18°W, the upper bound being 4.8 km. The glider IFM02 was deployed at 15.8°N–20.38°W and carried out 552 profiles from the surface to 900-m depth. Two sections were sampled: first, a southeastward 132-km-long section (D0; Figure 1), which reached the 14.7°N meridional transect at 19.92°W, and second, a westward 493-km-long transect at 14.7°N up to the Cape Verde archipelago at 24.5°W (D1; Figure 1). Both ascending and descending profiles were recorded during IFM02/DEPL21. The median horizontal resolution at 450-m depth (i.e., the middepth of the profiles) is about  $1.6 \pm 0.4$  km, the upper bound being 2.6 km. For comparison and quality control purposes, an 87-km-long overlapping section along 14.7°N between 19.92°W and 20.73°W was performed by both gliders.

Temperature and salinity were measured by an unpumped Sea-Bird conductivity-temperature-depth (CTD; SBE-41CP) mounted on the glider’s side. The CTD sensors had a temporal resolution of 0.5 Hz. With fall/climb rates of about 0.2 m/s, the typical vertical resolution is around 0.5 dbar. For processing purpose, the data were interpolated on a 1 dbar vertical grid.

On the *GLISEN* salinity measurements, a 0.03 pss (practical salinity scale, PSS-78) offset correction was applied (Figure S1 in the supporting information). This correction was necessary to adjust the mean salinity values (between 200- and 300-m depth) from colocated *GLISEN* and CTD casts at 14.71°N–17.65°W that were carried out during the AWA survey (Ecosystem Approach to the management of fisheries and the marine environment in West African waters), on board the French RV *Thalassa* (Ifremer), carried out the day of the *GLISEN* glider deployment. Differences linked to thermal inertia of the sensors were also observed in the salinity data between neighboring ascending and descending profiles (ascending and descending profiles were available for *GLISEN* only west of 18°W). These differences were corrected using thermal and time lag corrections applied to the conductivity, which minimized (in the least square sense) the difference between two successive ascending and descending  $\theta$ - $S$  profiles (Garau et al., 2011;

Pietri et al., 2013). The IFM02 temperature and salinity measurements were compared to a CTD cast during the deployment on RV Meteor M105 cruises (see Figure S2 in the supporting information). The temperature did not show any significant offset while salinity was corrected from a small offset ( $-0.011$  pss). The salinity error due to thermal inertia was corrected based on the method of Garau et al. (2011) and was improved by using a more accurate estimate of the glider dive and climb velocity (Thomsen et al., 2016). The comparison of GLISEN and IFM02  $\theta$ - $S$  profiles along the overlapping section did not reveal any significant differences (Figure S3 in the supporting information).

Both GLISEN and IFM02 dissolved oxygen measurements were made with an Aanderaa Optode 3835 mounted on the rear of the gliders. The IFM02 Optode was corrected for time response delays of the sensors and an in situ comparison with CTD- $O_2$  casts performed during the deployment (Hahn et al., 2014; Figure S2 in the supporting information) and was corrected from  $-3$   $\mu\text{mol/kg}$  offset. The IFM02 dissolved oxygen data were thus used as a reference to correct the GLISEN oxygen profiles. The GLISEN dissolved oxygen data were first computed from raw phase measurements. An average time response delay of the sensor was estimated by comparing raw phase measurements acquired during consecutive ascending and descending profiles at the beginning of the transect and then used to correct the raw phase data. The dissolved oxygen data were then recomputed using (i) these corrected phase measurements, (ii) temperature measurements from the CTD instead of the temperature measurements from the Optode (as recommended by Thierry et al. (2016) for the specific type of Optode sensor used on GLISEN), and (iii) the calibration parameters provided by the manufacturer. Last, the recomputed data were calibrated using the IFM02 dissolved oxygen data for the overlapping section. The adjustment of the GLISEN data to the IFM02 data on the overlapping section was performed following the Takashita et al. (2013) method, used for Argo dissolved oxygen correction, using a linear regression. This correction provided a reasonable agreement between both data sets (Figure S3 in the supporting information).

### 2.1.2. AVISO SLA and Surface Currents

To depict the regional geostrophic sea surface circulation, we used weekly maps of absolute dynamic topography and associated surface geostrophic currents as provided by Collecte Localisation Satellite-Space Oceanography Division of Toulouse, France. This delayed-time AVISO product, which merged various satellite altimeters, is distributed onto a  $0.25^\circ \times 0.25^\circ$  spatial grid. To determine the origin of the studied AC and its trajectory, an automatic eddy detection and tracking algorithm was applied to SLA maps (Chaigneau et al., 2008; Pegliasco et al., 2015) that better depicts the mesoscale field for this purpose. These maps, also delivered by AVISO, have the same spatiotemporal resolution than the maps of absolute dynamic topography product.

### 2.1.3. ISAS Product

To describe the large-scale distribution of shallow water masses in the ETNA, monthly fields of in situ temperature and salinity produced by ISAS (In Situ Analysis System, Gaillard et al., 2016) were used. The ISAS tool was mainly designed to map Argo profiles on standard 152  $z$  levels using optimal interpolation algorithm. Two typical interpolation scales were used to map the data; the first one is 300 km, corresponding to the nominal sampling target of the Argo network; the second corresponds to 4 times the local radius of deformation. In this study, the last release of ISAS products named ISAS15 (Kolodziejczyk et al., 2017) including delayed mode quality controlled Argo data was used.

## 2.2. Methods

The local first baroclinic mode Rossby radius of deformation is around 50 km in the ETNA (Chelton et al., 1998); therefore, the glider's density profiles were averaged every 1.5 days in the horizontal direction, generating a reduced number of averaged profiles typically spaced by  $\sim 20$ – $30$  km. Density was computed from temperature and salinity using McDougall and Ruddick (1992). The horizontally averaged profiles were used then to compute the geostrophic horizontal current perpendicular to the glider section using the thermal wind balance. Estimates of the vertically integrated horizontal velocities or depth-average currents (between the surface and the maximum depth of the dive) provided by the glider drift between two dives was projected in the direction perpendicular to the section. The vertically averaged velocities was also averaged every 1.5 days in order to filter out the barotropic tide currents ( $\sim 0.05$  m/s) during cruises. Then, it was used as reference, assuming that the vertically integrated velocity was mainly geostrophic due to a negligible contribution of near-surface Ekman velocity (Pietri et al., 2013).

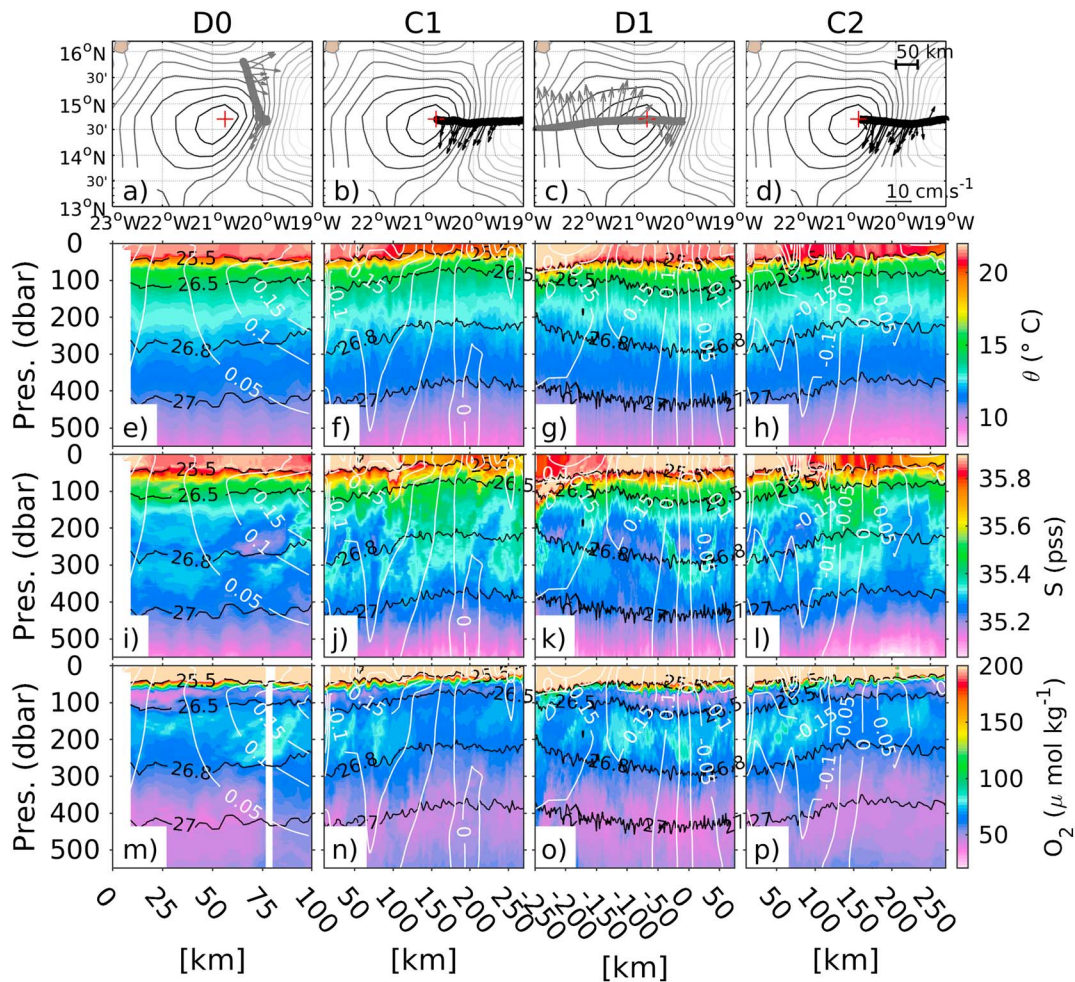


**Figure 2.** (a–d) AVISO absolute dynamic topography (in meters, confidence interval of 0.05 m; maximum is 0.35 m) in March 2014; trajectory (thick line) and glider depth averaged velocity (arrows) for (a) D0, (b) C1, (c) C2, and (d) C2 glider sections. Red cross indicate the center of the eddy as located along the 14.7°W glider sections (0 m/s mean velocity). (e–h) Potential temperature, (i–l) salinity, and (m–p) dissolved oxygen sections as a function of pressure (0–500 dbar) corresponding to each glider sections. Black contours mark potential density (in  $\text{kg/m}^3$ ). White contours mark the cross-section geostrophic velocity deduced from hydrology (in m/s). Transversal distance (in km) along the section is referenced from the zero vertical-averaged velocity, that is, the center of the AC (20.64°W–14.76°N).

To study the spatial distribution of fine-scale tracer features along the glider sections, the unbalanced motion, such as gravity waves, had to be filtered out (Cole & Rudnick, 2012). The procedure was the following: first, the isopycnal salinity and dissolved oxygen fields from sections D0, C1, C2, and D1 were reinterpolated on a 1-km resolution regular grid. Second, to compute the ratio of the vertical and horizontal gradient of small scale features, the isopycnal salinity and dissolved oxygen were 30 km high-pass filtered (HPF) with a Butterworth filter. Eventually, the HPF tracer fields were projected back in z coordinate using a 30-km low-pass filtered density field.

To further investigate the horizontal distribution of the tracer scales between 100- and 400-m depth, density spectra were computed for isopycnal salinity and dissolved oxygen in three isopycnal layers, namely, 25.5–26.6, 26.6–26.8 and 26.8–27.0  $\text{kg/m}^3$ , respectively (see black lines in Figure 2). Given the irregular sampling in the four different glider sections, ranging from 1 to 5 km, the minimum resolution retained was ~5 km; thus, the effective Nyquist scale was 10 km. To smooth the spectra and reduce its uncertainty, a spectral averaging procedure based on Welch algorithm using independent segments from C1, C2, D0, and D1 hydrological sections was used. In each isopycnal layer, three (eight) segments were extracted from the gliders sections (in a space domain) and windowed with a Hamming window. Based on the length of the section and the glider resolution, the corresponding spectra were averaged within the 100- to 33-km (33- to

10-km) wavelength range. This led to a degree of freedom of 3 (8), for salinity and dissolved oxygen. The confidence interval at 95% for the density spectra was estimated assuming a  $\chi^2$  distribution.

### 3. Results

#### 3.1. The Anticyclonic Glider Survey

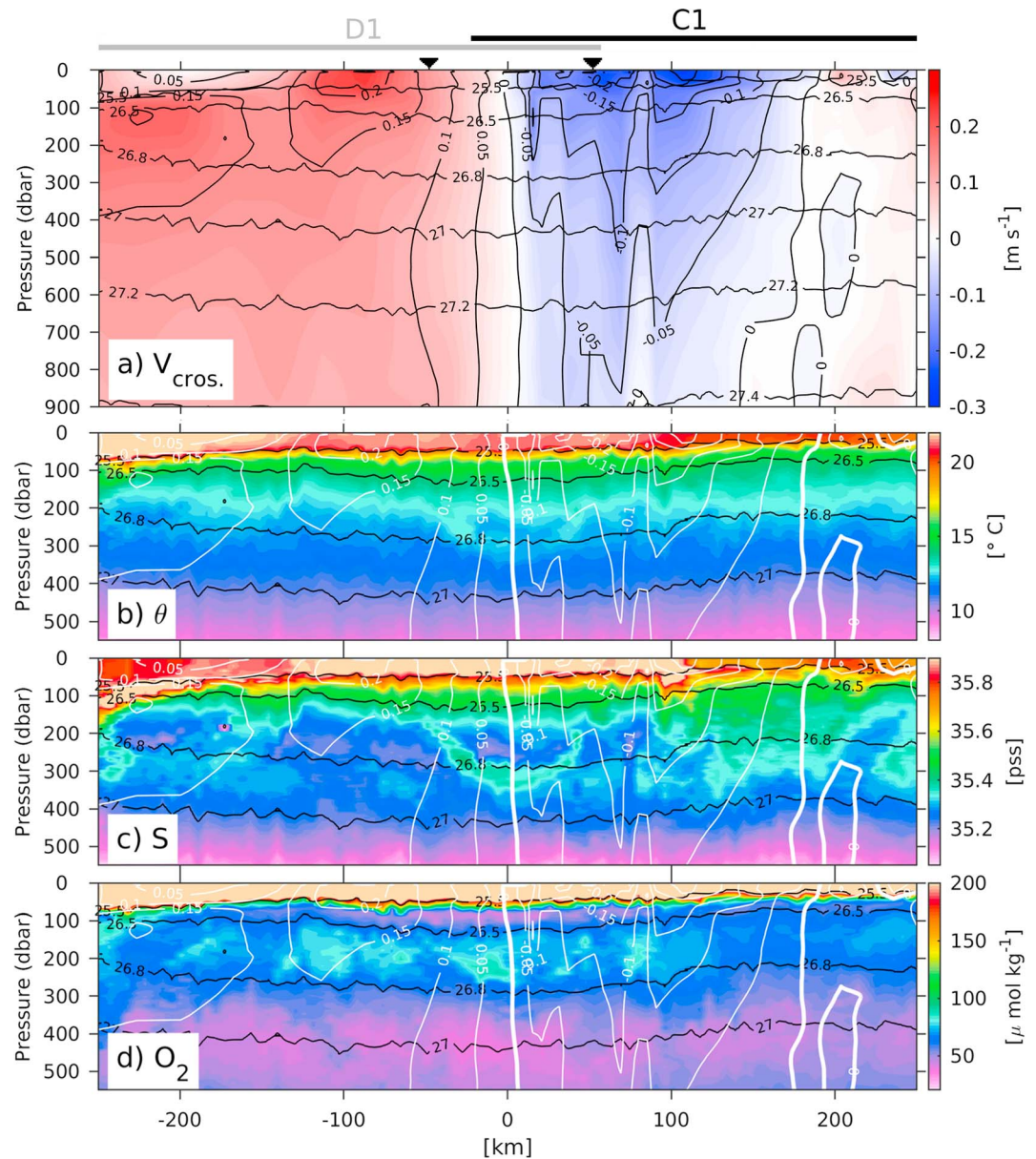
The AC was centered near 14.7°N–21.6°W in late March/early April 2014. Satellite data revealed surface geostrophic velocities of 0.2–0.3 m/s at the periphery of the AC and surface temperatures of 21–22 °C (Figures 1a–1c) at its center. The AC was located on the western side of a surface thermal front, which was positioned around 20°W (north-south oriented) with a magnitude of  $\sim 0.02$  °C/km (equivalent to 2 °C over a 100-km zonal distance). To the south, the eddy was separated from its surroundings by relatively cool water (20–21 °C; Figures 1a–1c) of coastal origin, which is advected around the eddy and offshore.

Figure 2 presents the location of the four sections, the depth averaged velocity along the sections, and the SLA associated with the AC (Figures 2a–2d). Section D0 was oriented north-south and sliced partially the northeastern part of the AC, while sections C1, D1, and C2 were oriented east-west, sampled the center of the AC, and provided a complete transversal section that crossed the eddy very near its center. The distance in D0, C1, C2, and D1 sections were referenced to the center of AC (0 km) and positive distances were eastward/northward. The center of the AC is referenced as the zero horizontal velocity measured by the glider drift along the section C1, C2, and D1 (20,74°W/14.7°N; Figure 2–2d, red cross; in Figure 2a, the 0-km reference along the meridional transect is taken to  $\sim 14.7^\circ\text{N}$ ). The isopycnal surfaces (black contours; Figures 2e–2p) deepened toward the center of the eddy suggesting a vertical shear of the horizontal cross-section currents. This was consistent with geostrophic velocity derived from the hydrological data (white contours; Figures 2e–2p) that revealed the circulation associated with the AC. A surface-intensified anticyclonic velocity of  $\sim 0.3$  m/s can be observed, in agreement with the surface geostrophic circulation as seen by altimetry. The joined surface altimetry maps and the four sections indicate that the AC was nonlinear ( $U/c > 1$ , where  $U \sim 0.3$  m/s is the maximum orbital velocity and  $c$  is the translation velocity near equal to 0), with an isolated eddy core located between the surface and about 600-m depth. A shallow thermocline halocline and oxycline (above 100 depth) were observed separating warm ( $> 20$  °C; Figures 2e and 2f), salty ( $> 35.8$  pss; Figures 2i–2l) and oxygenated ( $> 100$   $\mu\text{mol/kg}$ ; Figures 2m–2p) surface water, from cooler, fresher, and low oxygenated subsurface water. On the horizontal scale, the surface (upper 100-m depth of the AC) salinity and temperature signature of the AC were located between  $-150$  and  $100$  km from the center of the AC (Figures 2j–2l and 2f–2h). While the surface salinity anomaly represented a distinct maximum, the surface temperature anomaly associated to the AC was less clear. The water in the core of the AC was warmer than the near-shore water (further than  $150$  km from the AC center) but cooler than the western offshore water (further than  $-150$  km from the center of the AC).

In all temperature, salinity and dissolved oxygen sections, between 100- and 400-m depth and  $-150$  and  $100$  km from the center of the AC, the most striking features were the fine-scale sloped striations observed both in the salinity and dissolved oxygen sections (Figures 2i–2p), and to a lesser extent in temperature sections (Figures 2e and 2f). These salinity and dissolved oxygen fine-scale features exhibited horizontal scales of  $O(10\text{--}30$  km), smaller than those of the mesoscale eddy, that is,  $O(150$  km), and smaller than the local deformation radius, that is,  $\sim 50$  km (Chelton et al., 1998). The vertical scales of these features were  $O(5\text{--}100$  m) with an amplitude of  $\sim 0.2$  and  $\sim 40$   $\mu\text{mol/kg}$  for salinity and dissolved oxygen, respectively (Figures 2i–2p). Moreover, at the AC center between 150- and 350-m depth, a warm and saline *U-shaped* feature of  $\sim 100$ -m thickness and of  $\sim 100$ -km width was observed (Figures 2g–2k). Note that the fine-scale striations cross the isopycnals between  $26.5$  and  $27.0$   $\text{kg/m}^3$  (Figure 2). Before investigating these fine-scale contrasts of water masses, we first characterize in the next section the mesoscale structure of the AC, the origin of the water masses in its core, and the distribution of water masses in the region to better understand the origin of the water masses involved in such fine-scale features.

#### 3.2. The Mesoscale Structure

To better infer the mesoscale context of the AC, the cross-section velocities, temperature, salinity, and dissolved oxygen were reconstructed using C1 and D1 sections (Figure 3). The cross sections of geostrophic velocities from surface to 900-m depth revealed an east-west asymmetry (Figure 3a). The eastern part of



**Figure 3.** (a) Composite geostrophic meridional velocities (in  $\text{m s}^{-1}$ ) computed between 0 and 900 dbar and  $23\text{--}18^\circ\text{W}$ ; (b) composite potential temperature (in  $^\circ\text{C}$ ); (c) composite salinity (in psu); (d) composite dissolved oxygen (in  $\mu\text{mol/kg}$ ) between 0 and 550 dbar and  $23^\circ\text{W}\text{--}18^\circ\text{W}$  reconstructed from D1 and C1. Parameter  $\sigma_\theta = 25.5; 26.5; 26.8; 27 \text{ kg/m}^3$  contours are superimposed (solid thin black).

the AC, presented a moderate depth extension, showing southward velocities of only  $0.1 \text{ m/s}$  at  $400\text{-m}$  depth. In contrast, the western part of the eddy exhibited a more *barotropic* structure, with northward velocities of  $0.20 \text{ m/s}$  at the surface and larger than  $0.10 \text{ m/s}$  at  $900\text{-m}$  depth. Assuming an AC radius, being the distance from the center at which maximum orbital velocities can be observed, of around  $100 \text{ km}$  (Figures 3a–3d), the Rossby number defined as  $\text{Ro} = U_{\text{max}}/fR$  (where  $U_{\text{max}}$  is the maximum swirl velocity,  $f$  the Coriolis parameter and  $R$  the eddy radius) was  $\sim 0.08$  and the Burger number defined as  $\text{Bu} = (R_d/R)^2$  (where  $R_d = 60 \text{ km}$  is the first baroclinic Rossby radius of deformation; Chelton et al., 1998) was  $\sim 0.4$ . These values ( $\text{Ro} \sim 0.08$  and  $\text{Bu} \sim 0.4$ ) are thus characteristic of a quasi-geostrophic (QG) regime at the eddy scale.

Between the surface and  $100\text{-m}$  depth, the vertical distribution of temperature and salinity showed a relatively warm and salty eddy core between  $19.7^\circ\text{W}$  and  $22^\circ\text{W}$  (above  $15 \text{ }^\circ\text{C}$  and  $35.5 \text{ psu}$  along

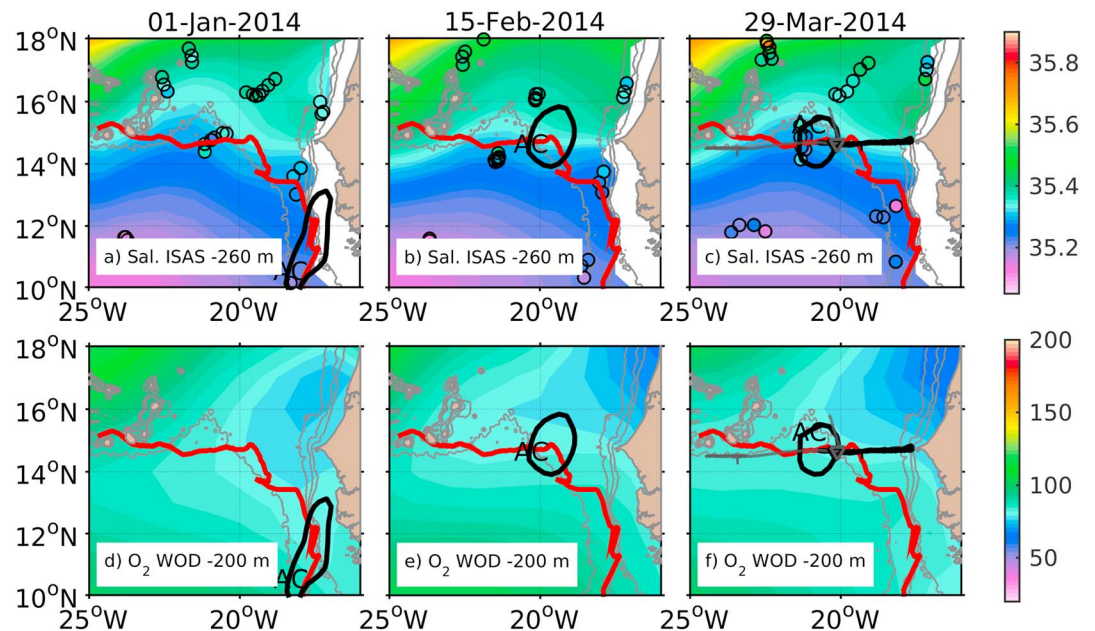
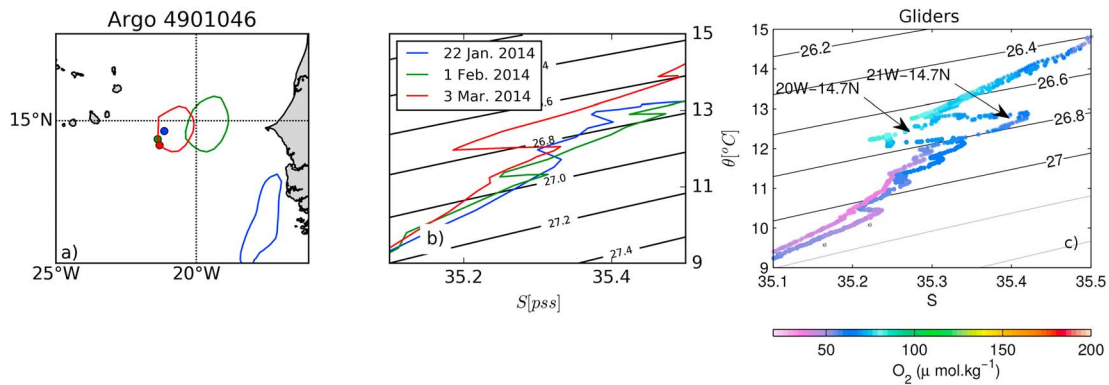


**Figure 4.** Salinity (in psu) at 260 m depth from ISAS monthly fields in (a) January 2014, (b) February 2014 and (c) March 2014. The positions of Argo float used for the analyses are superimposed (circles). Dissolved oxygen (in  $\mu\text{mol}/\text{kg}^3$ ) from WOD09 during climatological (d) January, (e) February, and (f) March. Red curve indicates the trajectory of the anticyclonic (AC) (black contours) as tracked by an eddy tracking method using AVISO altimetry (see text). The dates corresponding to the position of the AC are indicated in the title of each subfigure. In subfigure (c) and (f) the Gliders off Senegal (GLISEN; thick solid black) and DPL21 (thick solid gray) trajectories between March and May 2014 are plotted, and the actual positions of GLISEN (black triangle) and DPL21 (gray triangle) gliders on 29 March 2014 are marked.

$\sigma_\theta = 26.5 \text{ kg}/\text{m}^3$ ; between  $-100$  and  $100 \text{ km}$  in Figures 3b and 3c). In contrast, below the thermocline, between 100- and 300-m depth and between  $-100$  and  $100 \text{ km}$  within the core of the AC, salinity (and temperature to a lesser extent) was lower than near the edge of the AC. More precisely, east of the AC center, the southward current transported saltier water masses, while west of the AC center, the northward current transported a fresher water mass. The dissolved oxygen section (Figure 3d) exhibited two layers of low ( $<50 \mu\text{mol}/\text{kg}$ ) dissolved oxygen concentration: a thin layer located around 100-m depth and a thicker one below  $\sim 300$ -m depth. They were separated by a relatively oxygenated core ( $>80 \mu\text{mol}/\text{kg}$ ) located in the layer  $\sigma_\theta = 26.5\text{--}26.8 \text{ kg}/\text{m}^3$  (Brandt et al., 2015). In this density layer, between  $-100$  and  $100 \text{ km}$ , fine-scale dissolved oxygen features, characterized by positive anomalies of  $\sim 20\text{--}40 \mu\text{mol}/\text{kg}$  with respect to their surroundings, are associated with cooler and fresher fine-scale structures, while relatively warmer, saltier and less oxygenated features can be found somewhat deeper (Figures 3b–3d). The general picture suggests that the relatively warm, salty, and low-oxygenated smaller scale structures are embedded within the cooler, fresher, and oxygenated core of the anticyclone.

### 3.3. Water Masses in and Around the AC

To characterize the large-scale distribution of water masses surrounding the AC as well as the origin of the waters in the AC core, an eddy tracking algorithm was used to infer the eddy trajectory from altimetry. In Figure 4, the eddy position is plotted along with monthly ISAS salinity properties at 260-m depth. Each map of the Figure 4 panels corresponds to the monthly fields with Argo profiles available in January (Figure 4a), February (Figure 4b), and March 2014 (Figure 4c), respectively. In January, the AC originated southeast of the glider sections, near the African coast ( $10^\circ\text{N}\text{--}13^\circ\text{N}$ ). In this region, south of  $15^\circ\text{N}$ , SACW characteristics can be found. The SACW is a central water mass, with lower salinity than the northern NACW (Figure 4). The variations of large-scale salinity meridional gradients associated with the SACW and NACW, which form the Cape Verde Frontal zone (Zenk et al., 1991), were well captured at 260-m depth with the ISAS product. The AC was first found near-shore around  $10^\circ\text{N}\text{--}13^\circ\text{N}$  in early January as a meridionally stretched anticyclonic structure. It was located in a low salinity region at 260-m depth (around 35.3 pss;



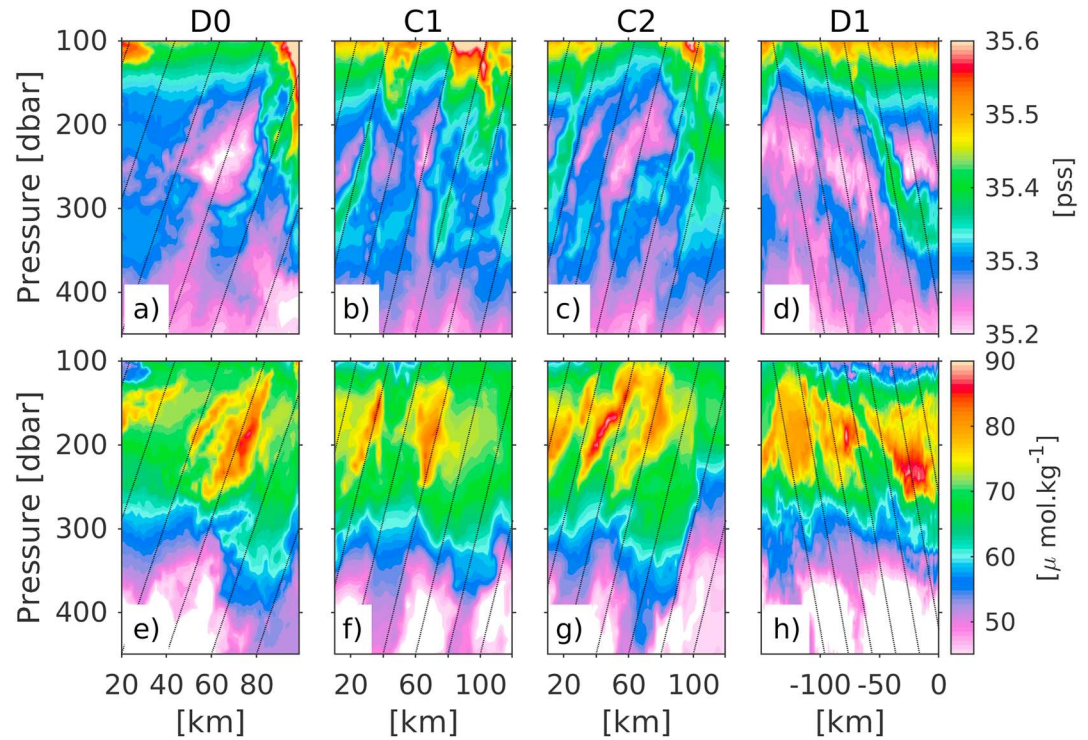
**Figure 5.** (a) Positions of Argo float WMO 4901046 (circles) and anticyclonic (contours) as deduced from altimetry on 22 January 2014 (blue), 1 February 2014 (green), 3 March 2014 (red). (b) Corresponding  $\theta$ - $S$  profiles from the Argo float. (c) Selected  $\theta$ - $S$  profiles within the anticyclonic at  $14.7^{\circ}\text{N}$ – $20^{\circ}\text{W}$  (circles) and  $14.7^{\circ}\text{N}$ – $21^{\circ}\text{W}$  (star). The location of these profiles is indicated by black triangles in Figure 3. Dissolved oxygen concentrations are indicated in color (in  $\mu\text{mol}/\text{kg}$ ).

Figure 4a) and in a more oxygenated region at 200-m depth ( $90 \mu\text{mol}/\text{kg}^3$ ; Figure 4d). Then, it moved northwestward and reached the location ( $14.6^{\circ}\text{N}$ – $21^{\circ}\text{W}$ ) where it was sampled by the gliders in February (Figure 4b). After February, it did not progress northward anymore and remained between the Cap-Vert peninsula and the Cape Verde islands (Figure 4c), in the region of strong meridional salinity gradient and above the topographic ridge between the Cape Verde Islands and the West African continent (Emery & Meincke, 1986). Fortunately, several Argo floats were present at the location of the AC during March 2014 (Figures 4a–4c). Thus, at 260-m depth, the March 2014 ISAS field displayed a salinity decrease around  $14^{\circ}\text{N}$ – $22^{\circ}\text{W}$  (Figure 4c), which can be explained by the northward migration of the salinity front on the western part of the AC, due to float sampling the eddy itself. The large-scale distribution of World Ocean Atlas 2013 climatological oxygen at 200-m depth (where the dissolved fine scale were found; Figure 3d) suggests that the eddy has been formed in a water mass of higher dissolved oxygen concentration than the NACW it encountered further north (Figures 4d–4f).

To get more insight in the water mass change due to the AC arrival in this region, the Argo float WMO 4901046 profiles were inspected (Figure 5a). They illustrated a water mass change after the arrival of the AC at around  $14.7^{\circ}\text{N}/21^{\circ}\text{W}$ . Within the isopycnal layer  $26.6$ – $27.0 \text{ kg}/\text{m}^3$  (corresponding to  $\sim 260$ -m depth), salinity decreased between January (Figure 5b, blue), February (Figure 5b, green), and March 2014 (Figure 5b, red), suggesting that the western AC northward velocities transported the SACW northward. Interestingly, in spite of relatively crude vertical resolution of the Argo profile (20 m between 200- and 400-m depth), between  $26.65$  and  $27.0 \text{ kg}/\text{m}^3$ , the Argo  $\theta$ - $S$  profile shows small vertical scale layering aligned with isopycnal contours (Figure 5b, red). This feature is generally related to density-compensated thermohaline small layers.

Two  $\theta$ - $S$  profiles glider measurements and associated dissolved oxygen properties within the AC core (Figure 5c) confirmed also the presence of fine-scale layers aligned with isopycnal surfaces, in the layer  $26.65$ – $27.0 \text{ kg}/\text{m}^3$ . Indeed, the glider profiles had a higher vertical resolution (about 1 m), which allowed it to resolve vertical scales that were not visible in the coarser vertical resolution of Argo profiles ( $\sim 20$  m). The layers thickness ranged from a few meters to several tens of meters and the glider profiles revealed that low (high) temperature/salinity features correspond to high (low) dissolved oxygen features. Several water masses were observed: the relatively fresh, cool and oxygenated SACW (at  $20^{\circ}\text{W}$ ;  $12^{\circ}\text{C}$ ,  $35.2 \text{ psu}$  and  $90 \mu\text{mol}/\text{kg}^3$ ; Figure 5c, see also Figure 3) and the saltier, warmer, and less oxygenated NACW (at  $21^{\circ}\text{W}$ ;  $12.5^{\circ}\text{C}$ ,  $35.4 \text{ psu}$  and  $50 \mu\text{mol}/\text{kg}^3$ , Figure 6). The contrasted water mass properties were associated with smaller-scale interleaving observed within the AC core (Figures 3 and 5).

To conclude this section, our in situ and satellite observations suggest that the AC transported low salinity, oxygenated SACW northward into the Cape Verde frontal zone ( $\sim 15^{\circ}\text{N}$ ) where NACW is found. At this location, at  $\sim 250$ -m depth, the AC velocity field is likely to have contributed to stir the meridional large-scale salinity and dissolved oxygen gradients. In addition, subsurface fine-scale interleaving, visible in both Argo and glider profiles, was observed and carried the water masses properties of both SACW/NACW. The subsurface fine-scale layering is investigated in more detail in the next section.



**Figure 6.** Isopycnal salinity for section (a) D0, (b) C1, (c) C2, and (d) D1 and isopycnal dissolved oxygen for section (e) D0, (f) C1, (g) C2, and (h) D1. Values are shown between 100- and 400-m depth. Dotted lines indicate the theoretical  $\mu N/f$  slope within the AC core (see text).

### 3.4. Fine-Scale Structure

#### 3.4.1. Tracer Layering

The isopycnal interpolation of the glider salinity and dissolved oxygen observations revealed a richness of fine-scale sloped striations (Figure 6). We estimated the slopes of the 30 km HPF sections as follows: the vertical and horizontal gradient are computed between 100 and 400 m, then a probability density function (PDF) was constructed for each section. The slope of the striations corresponded to the median of the PDFs. The median slopes of the fine-scale salinity features were  $5.4 \times 10^{-3}$ ,  $6.1 \times 10^{-3}$ ,  $5.8 \times 10^{-3}$ , and  $5.6 \times 10^{-3}$  from sections D0, C1, C2, and D1, respectively (Table 1). For dissolved oxygen, the median slopes were  $6.2 \times 10^{-3}$ ,  $8.1 \times 10^{-3}$ ,  $7.5 \times 10^{-3}$ , and  $5.5 \times 10^{-3}$  from sections D0, C1, C2, and D1, respectively (Table 1). Interestingly, the observed slopes of fine-scale striation are relatively close to the theoretical rescaled aspect ratio  $\mu f/N$  of the QG flow (dotted line, Figure 6; see section 3.4.3; Smith & Ferrari, 2009). The mechanisms that could explain the creation of such layers are investigated in the following sections.

#### 3.4.2. Double-Diffusion

Here we investigate the structure of two vertical profiles close to the center of the AC (approximately 0 km, 100- to 600-m depth range, Figures 3 and 8). The  $T$  and  $S$  200-m HPF profiles (Figure 7) were multiplied (dimensionalized) by the thermal expansion ( $\alpha$ ) and haline contraction ( $\beta$ ) coefficients, respectively, to relate their variations to density variations. The vertical profiles of temperature, salinity, and dissolved oxygen displayed layers with thickness of O(5–100 m) (Figures 7a–7d). The salinity and temperature profiles are highly correlated vertically (Figures 7a and 7b), resulting in a low vertical variability of the density field (Figure 7c), whereas the dissolved oxygen profiles illustrates they are anticorrelated with the salinity and temperature profiles.

The temperature and salinity contribution to the stratification was computed as follows:

$$-\frac{g}{\rho_0} \frac{\partial \sigma}{\partial z} = g\alpha \frac{\partial \theta}{\partial z} - g\beta \frac{\partial S}{\partial z} \quad (1)$$

where  $g$  is the acceleration of gravity and  $\rho_0 = 1,026 \text{ kg/m}^3$ , respectively. The left-hand side of (1) is the Brunt-Väisälä frequency ( $N^2$ ), the first term of the right-hand side (rhs) is the contribution of the temperature vertical

**Table 1**  
Estimated  $|\partial_x \Phi| / |\partial_z \Phi|$  From 30-km HPF Isopycnal Salinity and Oxygen Sections D0, C1, C2, and D1 (See Figure 6)

$f/N \sim 9 \cdot 10^{-3}$	D0	C1	C2	D1
Salinity median slope	$5.4 \times 10^{-3}$	$6.5 \times 10^{-3}$	$5.8 \times 10^{-3}$	$5.6 \times 10^{-3}$
Salinity slope 68th percentile	$2.9 \times 10^{-3}$	$3.5 \times 10^{-3}$	$3.4 \times 10^{-3}$	$3.1 \times 10^{-3}$
Salinity slope 32nd percentile	$1.0 \times 10^{-2}$	$1.2 \times 10^{-2}$	$1.0 \times 10^{-2}$	$1.0 \times 10^{-2}$
Oxygen median slope	$6.2 \times 10^{-3}$	$8.1 \times 10^{-3}$	$7.5 \times 10^{-3}$	$5.5 \times 10^{-3}$
Oxygen slope 68th percentile	$3.3 \times 10^{-3}$	$4.4 \times 10^{-3}$	$4.3 \times 10^{-3}$	$3.0 \times 10^{-3}$
Oxygen slope 32nd percentile	$1.1 \times 10^{-2}$	$1.5 \times 10^{-2}$	$1.3 \times 10^{-2}$	$1.0 \times 10^{-2}$

Note. The theoretical  $f/N$  ratio is indicated in the left upper corner.

gradient to the stratification ( $N_T^2$ ), and the second term of the rhs is the contribution of the salinity vertical gradient to the stratification ( $N_S^2$ ). Before computing Brunt-Väisälä frequency, the density, temperature, and salinity profiles have been smoothed with a Butterworth 10 m-low-pass filtered. The contribution of these gradients to stratification confirmed the density compensation (Figures 7e–7g).

The salinity had mainly a destabilizing effect ( $N_S^2 < 0$ ) against the stabilizing temperature vertical gradient ( $N_T^2 > 0$ ), except below salted filaments (e.g., ~260-m depth just above the salinity U-shaped feature; Figure 7b and 7c) where salinity had a stabilizing effect (Figure 7f) and temperature a destabilizing effect (Figure 7e). The Turner angle (Tu) is another index to quantify the contribution of temperature and salinity vertical gradient to the stable vertical stratification (Ruddick, 1992):

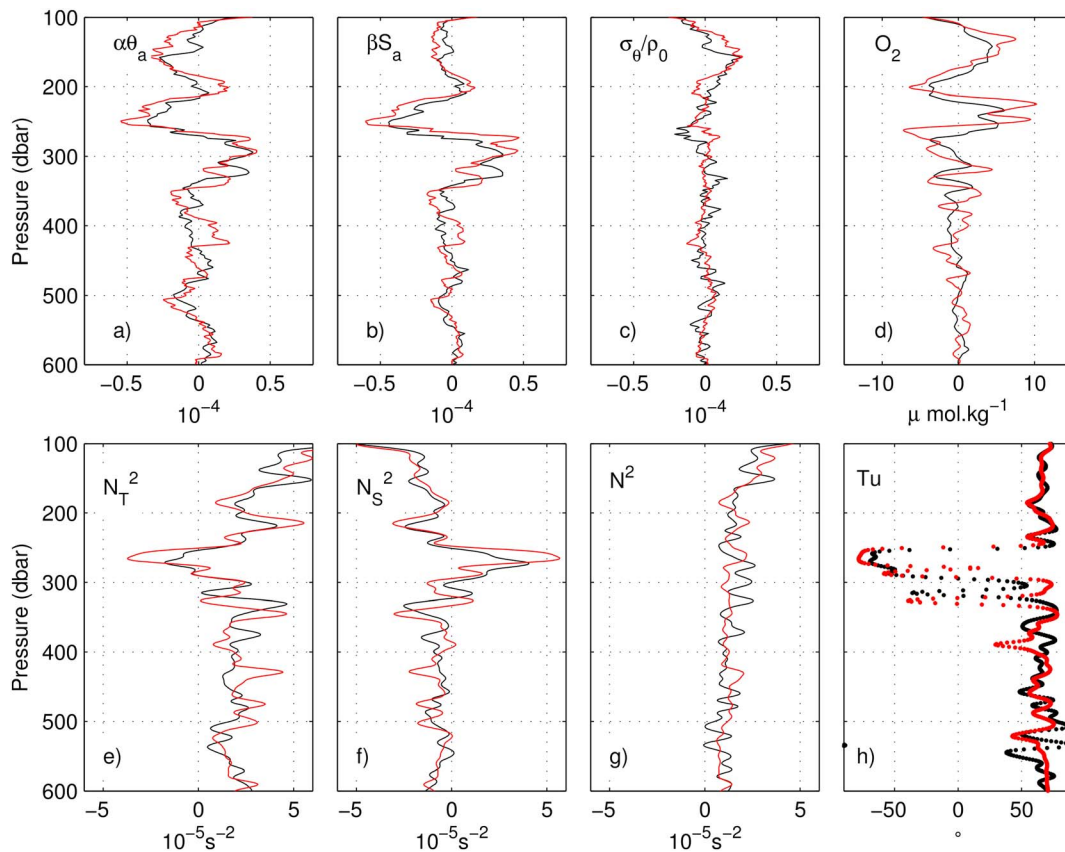


**Figure 7.** Vertical profiles from Gliders off Senegal (black) and DEPL21 (red) of 200-m high-pass filter adimensionalized temperature (a), salinity (b), and density (c) within the anticyclonic (at 20.7°W–14.7°N). The adimensionalization is done by multiplying  $\theta$  by  $\alpha$  the thermal expansion coefficient, and  $S$  by  $\beta$  the haline contraction coefficient, and scaling by  $\rho_0 = 1,026 \text{ kg/m}^3$ , respectively. (d) Vertical profiles of 200-m high-pass filter dissolved oxygen concentration (in  $\mu\text{mol/kg}$ ). Contributions of temperature (e) and salinity (f) to the Brunt-Väisälä frequency (in  $\text{s}^{-2}$ ). (g) Brunt-Väisälä frequency (in  $\text{s}^{-2}$ ). (h) Turner angle (in degrees).

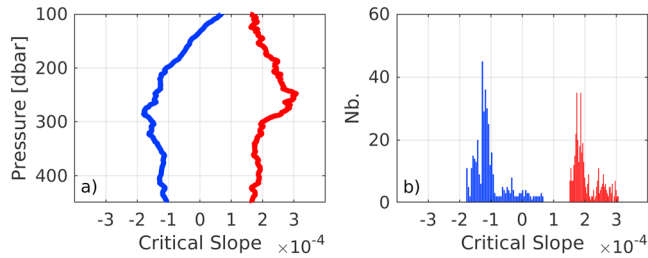


**Figure 8.** (a) Vertical structure of the critical slopes for double-diffusion derived from the mean  $\theta$ - $S$  profiles within the western (blue) and eastern (red) parts of the anticyclonic (AC). (b) Histogram of the critical slopes for double-diffusion within the western (blue) and eastern (red) part of the AC between 100- and 400-m depth and  $-100$  and  $100$  km from the center of AC.

$$Tu = \arctan\left(\frac{\alpha\theta_z + \beta S_z}{\alpha\theta_z - \beta S_z}\right) \quad (2)$$

If  $-45^\circ < Tu < 45^\circ$ , both temperature and salinity vertical gradients are stabilizing; if  $Tu > 45^\circ$  ( $Tu < -45^\circ$ ), the temperature vertical gradient is stabilizing (destabilizing) while the salinity vertical gradient is destabilizing (stabilizing). Furthermore, a Turner angle greater (less) than  $72^\circ$  ( $-72^\circ$ ) is a necessary condition for double diffusive salt fingering (double diffusive convection). In the AC profiles,  $|Tu|$  was larger than  $50^\circ$  over the major part of the water column (Figure 7h), indicating possible double diffusion.  $Tu$  was generally positive and typical of the possibility of double diffusive salt fingering salinity except around 260-m depth where, the  $Tu$  angle was strongly negative ( $Tu \sim -70^\circ$ – $80^\circ$ ), indicative of a possible double diffusive-convective regime (St Laurent & Schmitt, 1999, You, 2002; Ruddick, 1992).

As pointed out by May and Kelley (1997), the high absolute values of the Turner angle are not a sufficient condition for double diffusion, especially in baroclinic eddies where vertical shear can enhance or suppress double diffusion. Linear analysis from May and Kelley (1997) indicated that the criterion for double diffusive instability is actually satisfied if

$$s < \frac{\epsilon_z \bar{S}_x / \bar{S}_z + \bar{\rho}_x / \bar{\rho}_z}{(\epsilon_z + 1)} \quad (3)$$

where  $s$  is the slope for double diffusive layering, that is, the slope of the tracers (salinity or dissolved oxygen) layering along a AC transversal section, and  $\epsilon_z$  is a nondimensional quantity depending on density ratio,  $R_\rho$ , and a double diffusive flux parameter,  $\gamma_f$ .  $\epsilon_z \equiv (1 - \gamma_f) / (R_\rho - 1)$ ; chosen to be  $\gamma_f \sim 0.7$  (McDougall & Ruddick, 1992). The critical slope,  $s$ , is also the most likely observable tracer slope given a background tracer gradient and velocity shear. To compute the background salinity and temperature gradients, the salinity ( $S$ ) and density ( $\bar{\rho}$ ) background profiles were computed by averaging the profiles over three regions (see Figure 3): the western part of the AC within  $-250$  and  $100$  km, the AC core within the  $-100$  and  $100$  km, and the eastern part of the AC within  $100$  and  $250$  km. These three averaged profiles are assumed to be representative of the mean background profile of salinity and density. These averaged profiles are used to compute the vertical and horizontal derivative in rhs of equation (3). Between 100- and 400-m depth, the median value of the critical slope ( $s$ ) for western and eastern part of the AC were  $-1.1 \times 10^{-4}$  and  $2 \times 10^{-4}$ , respectively (Figure 8b). The signs of these slopes were similar to the signs of slopes on both western and eastern side of the AC (Figure 8a), but the magnitudes of the slopes were significantly smaller than the observed salinity and dissolved oxygen slopes (Figure 7 and Table 1), which ranged between  $5.5 \times 10^{-3}$  and  $8.1 \times 10^{-3}$  in absolute value. Therefore, double diffusion is unlikely to explain the generation of striations wrapped around the AC core between 100- and 400-m depth. However, right at the center of the AC around 300-m depth, in the center of U-shaped thermohaline structure, a nearly flat slope is observed ( $\sim 0$  km; Figure 3c). This is the only location where the nearly flat slope of a thermohaline fine-scale feature might be compatible with the critical slope value of double diffusion.

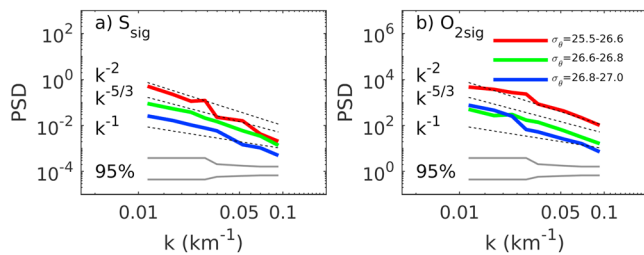


**Figure 9.** Density power spectra of isopycnal salinity (a) and dissolved oxygen (b) between  $18^\circ$ W and  $23^\circ$ W (C1, C2, D1 sections) within the  $\sigma_\theta = 25.5$ – $26.6$  (red),  $26.6$ – $26.8$  (green), and  $26.8$ – $27$  (blue)  $\text{kg/m}^3$  isopycnal layers. The  $k^{-1}$ ,  $k^{-5/3}$ , and  $k^{-2}$  slopes are superimposed (dashed lines). The 95% confidence interval is indicated by gray solid lines.

### 3.4.3. Stirring

To get more insight into the horizontal distribution of fine-scale tracers between 100- and 400-m depth, the density spectra of isopycnal salinity and dissolved oxygen were computed for sections D0, C1, C2, and D1 (Figure 9). The isopycnal salinity and dissolved oxygen have relatively similar spectral characteristics reflecting that salinity and dissolved oxygen can be considered as quasi-conserved quantities at depths greater than 200 m and at time scales of a few days (Karstensen et al., 2008). The spectra slopes ( $k^\alpha$ ) were estimated following two different methods: (i) a linear fitting on the spectrum was computed over the 10- to 100-km length scale range and (ii) following the methodology from Itoh and Rudnick (2017). The results were consistent and the uncertainty could be estimated. For the

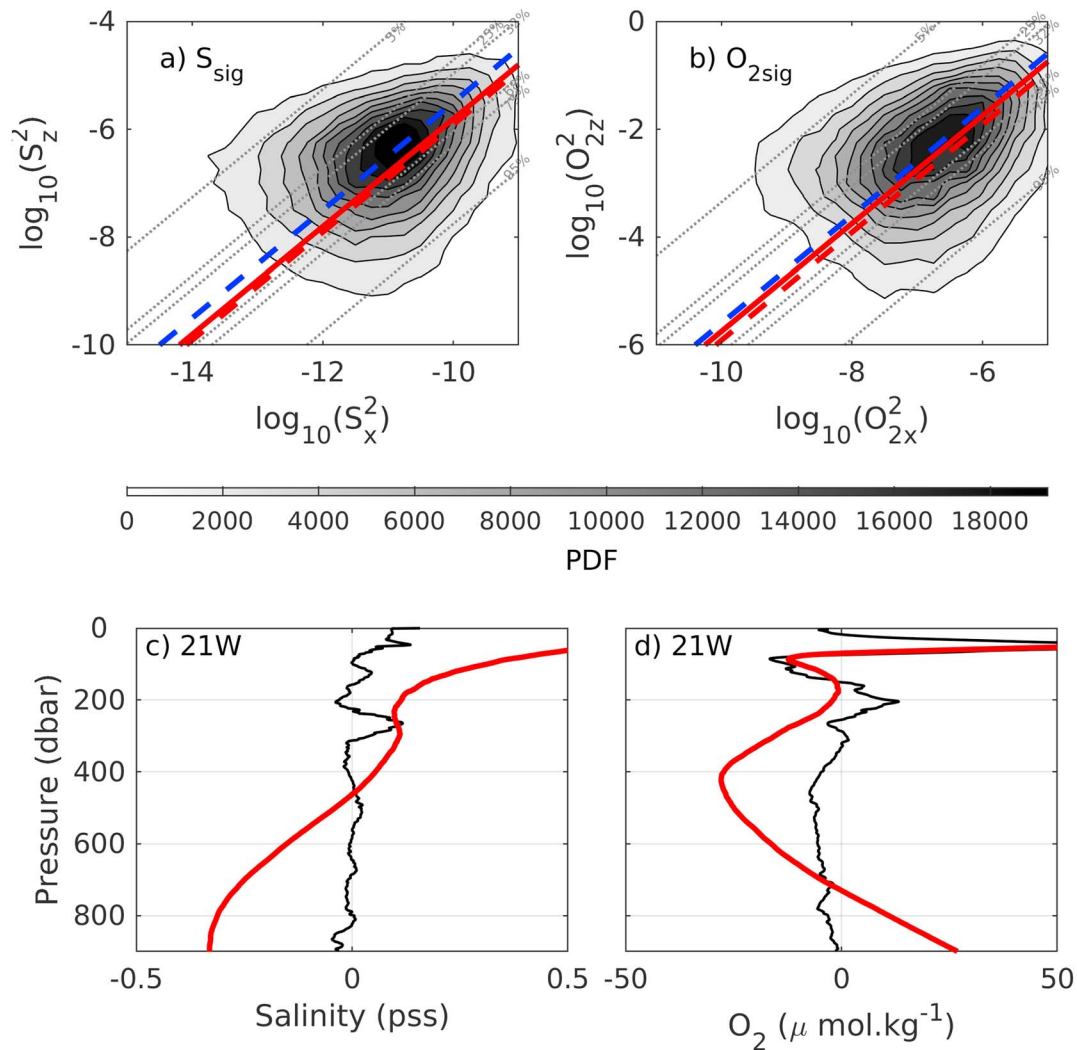


**Figure 10.** Joint PDFs of the zonal and vertical gradients of isopycnal salinity (a) and odissolved oxygen (b) computed from the 30-km HPF D0, C1, C2, and D1 section shown in Figure 6. Lines mark the theoretical aspect ratios: The  $N/f$  ratio (red dashed), the rescaled  $N/f$  ratio (see equation (2); red solid) and estimated local median ratio of tracers vertical and horizontal gradients (blue dashed). Dotted gray lines represent the 5th, 25th, 32th, 68th, 75th, and 95th percentiles of slope distribution. (c) Salinity (in psu) and (d) dissolved oxygen (in  $\mu\text{mol}/\text{kg}$ ) mean profiles (thick red) and deviations from the mean profiles (thin black) at  $14.7^\circ\text{N}$ – $21^\circ\text{W}$ . The mean profiles were obtained by (i) averaging over the composite section shown in Figure 3 and (ii) by removing the vertical average of the mean profile.

layer  $26.6$ – $26.8 \text{ kg}/\text{m}^3$  (where fine-scale features are located), the spectra linear fit led to values of  $-2.0 \pm 0.4$  and  $-1.7 \pm 0.3$  (with a confidence level at 99%) for salinity and oxygen, respectively, while using spectral ratios, the median values for spectral bands within  $[100\text{--}10] \text{ km}$  were around  $-1.9$  and  $-2.1 \pm 3.4$  (with a confidence level at 90%). Considering the uncertainty due to the limited number of sections across the AC, the spectral slopes are compatible with two different regimes: the stirring of tracers by mesoscale eddies, leading to spectral slopes of  $k^{-2}$  (Ferrari & Polzin, 2005) in a QG regime, and the geometric distribution of tracers due to spiral advection, leading to  $k^{-5/3}$  in a vortex lens (Gilbert, 1988; Hua et al., 2013).

In the absence of heat flux, freshwater flux, and mixing, potential vorticity conservation suggests that the vertical scales may be linked to the horizontal scales of the tracer field because of the stirring by the mesoscale eddy velocity field. In QG dynamics, passive tracers (such as assumed here isopycnal salinity and dissolved oxygen) are sheared and strained by the mesoscale velocity field, leading to an aspect ratio (i.e., ratio of vertical to horizontal scales) close to  $f/N$  (Smith & Ferrari, 2009). A joint PDF for vertical and horizontal gradients of salinity and dissolved oxygen between 100- and 400-m depth was computed from D0, C1, C2, and D1 sections (Figures 10a and 10b, shading and blue dashed line) and compared with the theoretical slope ( $f/N$ ), computed from the mean stratification within the AC between 100- and 400-m

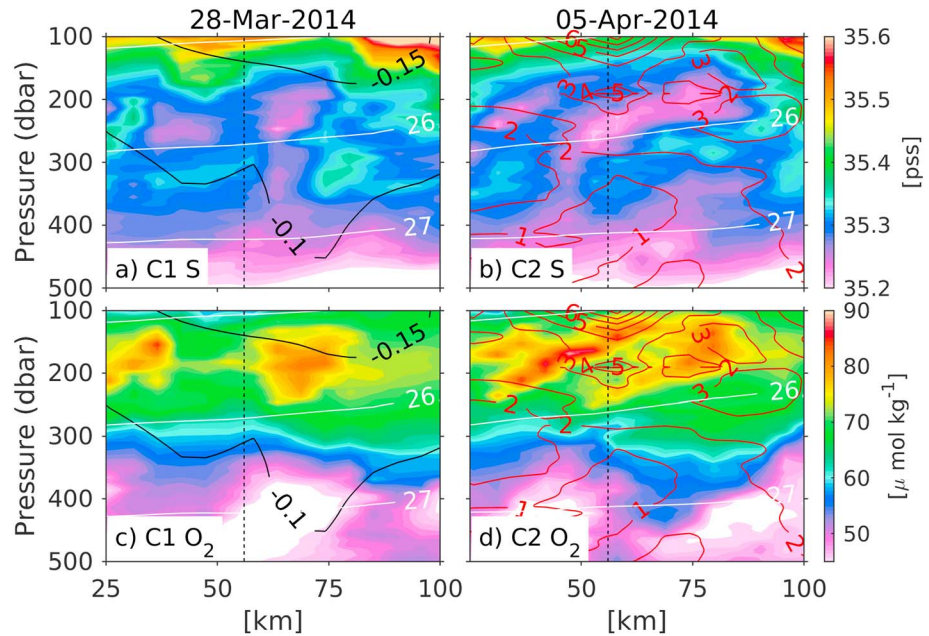


**Figure 11.** (a and b) Isopycnal salinity (in psu) and (c and d) dissolved oxygen (in  $\mu\text{mol/kg}$ ) for C1 (a and c) and C2 (b and d) Gliders off Senegal sections within 25- to 100-km and 100- to 500-m depth. Black contours are (a and b) cross-section geostrophic velocity (in m/s). Red contours (d and c) are the cross section current vertical shear (in  $10^{-4}/\text{s}$ ). The dashed vertical line marks the position of the glider at the date indicated in the title of the subfigures.

depth ( $f/N \sim 9 \times 10^{-3}$ , Figures 10a and 10b, red dashed line). The slope derived from the salinity and dissolved oxygen gradients was close to the theoretical slope  $f/N$  but did not match it exactly. This could be explained by the dispersion of the individual slope observed values and by the trajectory of the glider, which likely did not cross the small scale filaments always perpendicularly, which may lead to an underestimation of the slopes. Moreover, the conditions of the observed AC differed from the observations and numerical experiments presented in Smith and Ferrari (2009). In regions where tracers have a rich vertical structure, as in the case of a fine-scale tracer vertical gradient superimposed to a large-scale background tracer vertical gradient, it is difficult to evaluate precisely the slope of filaments. In our case, fine-scale features were located within a surface intensified AC in which a substantial background vertical gradient of the tracers (halocline and oxycline) was found (Figure 3). In this context, Smith and Ferrari (2009) suggested that the tracers aspect ratio should be rescaled as follows:

$$\mu = |1 + h_{\text{filament}}/h_{\text{background}}| \quad (4)$$

where  $h_{\text{filament}}$  and  $h_{\text{background}}$  are scalings for the thickness of a fine-scale filament and of the background tracer gradient, respectively. The  $h_{\text{filament}}$  and  $h_{\text{background}}$  scales were estimated using average values of  $(\Phi \frac{\partial \Phi}{\partial \Phi})$  and  $(\Gamma \frac{\partial \Gamma}{\partial \Gamma})$ , respectively (Smith & Ferrari, 2009), where  $\Phi$  is the tracer fields distribution in the presence of the background vertical tracer gradient and  $\Gamma$  is the vertical background distribution of tracer. In the presence of background tracer structure ( $\mu > 1$ ) the aspect ratio is in fact larger than when no background vertical tracer gradient is present. In the present case, values of  $\mu$  were estimated using the mean salinity and dissolved oxygen profiles (averaged in the AC between  $19^\circ\text{W}$ – $22^\circ\text{W}$ ; Figures 10c and 10d). On average between 100- and 300-m depth and within the AC core, we found  $h_{\text{background}} \sim O(150)$  m ( $\sim O(100)$  m) and  $h_{\text{filament}} \sim O(20)$  m ( $\sim O(20)$  m) for salinity (dissolved oxygen). This leads to a factor  $\mu$  around  $1.13 \pm 0.05$  ( $1.2 \pm 0.82$ ) for salinity (dissolved oxygen) tracer. The rescaled theoretical ratios ( $f/\mu N$ ) were equal to  $8.1 \times 10^{-3}$  and

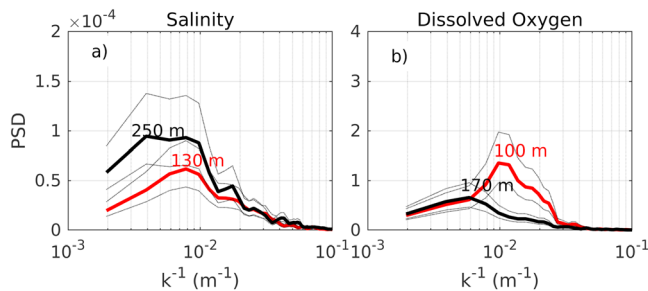


**Figure 12.** Variance preserving spectra computed for vertical scales of (a) salinity and (b) dissolved oxygen from C1 (black; ~28 March 2014) and C2 (red; ~5 April 2014) sections within 25- to 100-km and 100- to 400-m depth for the 30-km high-pass filter tracers fields. Dotted curves mark the 95% confidence interval.

$7.5 \times 10^{-3}$  (Figures 10a and 10b, red line) for salinity and dissolved oxygen respectively, thus in slightly better agreement with the observed ratios. However, this effect was small and did not fully explain the deviation of the observed slope from the theoretical slope  $f/N$ .

Another explanation for the observed slope discrepancies could be that the glider did not cross the fine-scale features with a trajectory parallel to that of the maximum slope. Indeed, the front direction and the vertically integrated velocity made an angle of  $\sim 30^\circ$  with the direction perpendicular to the glider section (Figures 2a–2d). Therefore, if we speculate that the glider crossed the fine-scale structure with an angle of  $\sim 30^\circ$ , the horizontal tracer gradient would be underestimated by a factor of  $\cos(30^\circ)$  ( $\sim 87\%$ ) leading to underestimated aspect ratios. This would imply that observed values for the slope of  $5.4\text{--}6.5 \times 10^{-3}$  for salinity (and  $5.5\text{--}8.1 \times 10^{-3}$  for dissolved oxygen) would be in reality  $\sim 6.2\text{--}7.5 \times 10^{-3}$  for salinity ( $\sim 6.3\text{--}9.5 \times 10^{-3}$  for dissolved oxygen), which seems more in agreement with the theoretical values of  $8.1 \times 10^{-3}$  ( $7.5 \times 10^{-3}$  for dissolved oxygen). This suggests that a significant part of the discrepancies between the observed values and the theory could be due to that effect.

Another source of discrepancy is that the filaments elongation by stirring may evolve in time as suggested by the numerical simulations of Meunier et al. (2015). More precisely, the vertical layer thickness could diminish as a function of time. In our observations, the eastern side of the AC (i.e., east of  $20.5^\circ\text{W}$ ) was sampled twice at different dates (C1 and C2 sections, and there were 8 days between the two passages at  $20.1^\circ\text{W}/55$  km from the center; dotted line in Figures 11a–11d), which allowed to observe the time evolution of some of the observed structures. The two sections revealed a surface intensified southward velocity (Figures 11a and 11c, black contours), that is, a significant vertical shear of the southward velocities around  $20.1^\circ\text{W}/55$  km from the center (Figures 11b and 11d, red contours). Between 100- and 300-m depth and around 56 km from the center of the eddy, the salinity and dissolved oxygen fine-scale features located on the eastern side of AC intensified (Figures 11a–11d). The sloping fine-scale features were embedded in an intensified vertical shear of the horizontal velocity between 28 March and 5 April. The evolution of maximum values of spectral estimates of vertical scales (Figure 12) showed a decrease of the vertical scales from  $\sim 250$  ( $\sim 170$ ) m to  $\sim 130$  ( $\sim 100$ ) m (Figure 12) for salinity (dissolved oxygen), possibly induced by the strong vertical shear of the horizontal flow (Meunier et al., 2015). The reduction of the vertical scale with time is thus likely to reduce the slope of the fine-scale tracer striations as observed between C1 and C2 salinity ( $6.5 \times 10^{-3}$  to  $5.8 \times 10^{-3}$ ; Table 1) and dissolved oxygen sections ( $8.1 \times 10^{-3}$  to  $7.5 \times 10^{-3}$ ; Table 1).

#### 4. Discussion and Conclusions

Glider measurements provide unprecedented high-resolution insight into the processes involved in thermohaline and dissolved oxygen layering and stirring, induced by mesoscale eddies. A 300-km-wide AC was sampled off Cap-Verde peninsula by two gliders during March–April 2014. It was tracked back close to the coast in the southeastern region of the ETNA few months before. After its generation near the coast the oxygenated isolated eddy moved poleward, transporting water masses of Southern Hemisphere origin (SACW) in its core. At the time it was sampled, the AC was located in the meridional large-scale thermohaline gradient associated with the Cape Verde Front and within the upper (10- to 300-m depth) OMZ (Brandt et al., 2015; Karstensen et al., 2008). Mesoscale advection, stirring, layering, and vertical shear of the azimuthal velocity within the AC core are found to have partially created fine-scale features of temperature, salinity, and dissolved oxygen, favoring a cascade toward fine-scale mixing and diffusion. These observed stirred features provide important knowledge that are especially useful to evaluate the realism of fine-scale processes in numerical models and improve their parameterizations.

Considering the irregular horizontal sampling of the gliders, which ranged between 1 km and 5 km, the fine scales within this range were poorly resolved. Thus, we chose to disregard scales smaller than 5 km and focus on the subsurface fine-scale features with scales around 10–30 km located below the thermocline between 100- and 400-m depth. This length scale can be considered as submesoscale since it is smaller than the local Rossby radius ( $\sim 50$  km). Indeed, the 5-km sampling scale prevented us to fully resolve the mixed layer submesoscale dynamics, which may be less than 1 km in the mixed layer (Rudnick & Martin, 2002). Furthermore, in spite of corrections (see section 2.1.1), the measurement around the thermocline ( $\sim 100$ -m depth) may be less accurate. In any case, the study of submesoscale mechanisms in the surface mixed

layer are at the limits of the experiment sampling (e.g., Brannigan, 2016; Du Plessis et al., 2017; Mahadevan et al., 2012; Thompson et al., 2016) and thus beyond the scope of this work.

The present study is in line with several previous studies in ETNA and other ocean basins about water mass structures in eddy cores (e.g., Cole & Rudnick, 2012; Pietri et al., 2013; Pietri & Karstensen, 2018). Various interleaving structures at different locations and depths were described in these works. Along isopycnal layers in the interior central North Pacific subtropical ocean, Cole and Rudnick (2012) found isopycnal salinity spectral slope of the order of  $k^{-2}$  in the permanent thermocline (Cole et al., 2010). Callies and Ferrari (2013) also found a spectral slope of  $k^{-2}$  in the northeastern subtropical Pacific region but outside of eddies. In contrast, stirring of tracer fields in an isolated, stratified eddy may result in typical  $k^{-5/3}$  and  $k^{-2}$  spectral slopes in QG theory, corresponding to a spiral advection of tracer (Gilbert, 1988; Hua et al., 2013). In the present study, the isolated AC may exhibit some characteristics of this latter dynamical regime: a small Rossby number compatible with QG framework and isopycnal tracer spectra slope around  $k^{-1.9}$ . The fine-scale structures below the thermocline could thus be explained by the stirring of relatively salty NACW by the mesoscale current associated with an AC in the vicinity of the Cape Verde front.

Using observations and numerical experiments, Meunier et al. (2015) simulated the evolution of a passive tracer field stirred by an idealized azimuthal, vertically sheared velocity field associated with a mesoscale eddy. As noted in Smith and Ferrari (2009) and Meunier et al. (2015), a critical ingredient for mesoscale stirring and layering is the presence of vertical shear of the eddy orbital velocity, which was particularly strong in the eastern part of our studied AC. Indeed, in glider section C1 and C2 (Figure 11), the velocity field exhibited vertical shear, and an aspect ratio of fine-scale layering, which are consistent with the QG stirring theory (Smith & Ferrari, 2009). In contrast, on the western side of the AC where the horizontal currents were more barotropic (section D1, Figures 2 and 3), the layers seem slightly less oriented along  $f/N$  slopes, thus less consistent with stirring theory (Figures 6c and 6g). Besides, the different background vertical gradients for dissolved oxygen and salinity may partly explain the slight difference of aspect ratio observed between the dissolved oxygen and salinity tracers. On the other hand, it is suggested that the inviscid QG theory may not explain the whole story of the fine-scale stirring and layering within an eddy, as it is difficult to match exactly the slope of fine-scale striations with those predicted from QG theory. Mixing and diffusive processes may also impact the slope scales. A better description of the 3-D velocity and tracer field is needed to further quantify the mechanisms at stake, which cannot be fully explored from only two gliders operating at the same time.

Finally, this study confirms that glider technology may enable an efficient monitoring of regions of the ocean characterized by strong variability at scales less than the mesoscale but that are nevertheless very important at global scale. As outlined in Liblik et al. (2016) underwater glider fill an important time/space sampling segment in ocean observing systems. To better understand regional ocean dynamics, observations are required at a higher spatial and temporal resolution than those typical of the Global Ocean Observing System, such as the Argo array (300 km; 10 days, Gould et al., 2004). A complementary glider deployment strategy may be especially relevant in marginal seas, in coastal as well as boundary current regions.

## References

- Alpers, W., Brandt, P., Lazar, A., Dagorne, D., Sow, B., Faye, S., et al. (2013). A sub-mesoscale oceanic eddy off the coast of West Africa studied by multi-sensor satellite and surface drifter data and by numerical modeling. *Remote Sensing of Environment*, *129*, 132–143. <https://doi.org/10.1016/j.rse.2012.10.032>
- Aristegui, J., Barton, E. D., Alvarez-Salgado, X.-A., Santos, A. M. P., Figueiras, F. G., Kifani, S., et al. (2009). Sub-regional ecosystem variability in the Canary current upwelling. *Progress in Oceanography*, *83*(1–4), 33–48.
- Banyte, D., Visbeck, M., Tanhua, T., Fischer, T., Krahnmann, G., & Karstensen, J. (2013). Lateral diffusivity from tracer release experiments in the tropical North Atlantic thermocline. *Journal of Geophysical Research: Oceans*, *118*, 2719–2733. <https://doi.org/10.1002/jgrc.20211>
- Brandt, P., Banyte, D., Dengler, M., Didwischus, S.-H., Fisher, T., Greatbatch, R. J., et al. (2015). On the role of circulation and mixing in the ventilation of oxygen minimum zones with a focus on the Eastern tropical North Atlantic. *Biogeosciences*, *12*(2), 489–512. <https://doi.org/10.5194/bg-12-489-2015>
- Brandt, P., Hormann, V., Körtzinger, A., Visbeck, M., Krahnmann, G., Stramma, L., et al. (2010). Changes in the ventilation of the oxygen minimum zone of the tropical North Atlantic. *Journal of Physical Oceanography*, *40*, 1784–1801. <https://doi.org/10.1175/2010JPO4301.1>
- Brannigan, L. (2016). Intense submesoscale upwelling in anticyclonic eddies. *Geophysical Research Letters*, *43*, 3360–3369. <https://doi.org/10.1002/2016GL067926>
- Callies, J., & Ferrari, R. (2013). Interpreting energy and tracer spectra of upper-ocean turbulence in the submesoscale range (1–200 km). *Journal of Physical Oceanography*, *43*, 24562–24474. <https://doi.org/10.1175/JPO-D-13-063.1>
- Capet, X., Estrade, P., Machu, E., Ndoye, S., Grelet, J., Lazar, A., et al. (2017). On the dynamics of the southern Senegal upwelling center: Observed variability from synoptic to superinertial scales. *Journal of Physical Oceanography*, *47*(1), 155–180. <https://doi.org/10.1175/JPO-D-15-0247.1>

## Acknowledgments

Nicolas Kolodziejczyk was supported by a CNES postdoctoral grant and by the ESA SMOS+SOS project. The GLISEN project was supported by the french national programme LEFE/INSU received funding from the EU FP7/2007-2013 under grant agreement 603521. The GLISEN glider, named CAMPE, was prepared with the support of DT-INSU (Ifremer, Toulon, France). GEOMAR's IFM02 deployment was funded jointly by the German Federal Ministry of Education and Research (BMBF) as part of the project AWA (01DG12073E) and by the Deutsche Forschungsgemeinschaft through the Collaborative Research Centre "SFB 754." The AWA survey was funded by the AWA project (BMBF-IRD). MODIS SST maps were provided by NASA oceancolor project and are freely downloaded from <http://oceancolor.gsfc.nasa.gov/>. Raw data are freely available on Coriolis Data center: <http://www.coriolis.eu.org/Data-Products/Data-Delivery/Data-selection>. The altimeter products were produced by Ssalto/Duacs and distributed by Aviso, with support from Cnes (<http://www.aviso.altimetry.fr/duacs/>). The AVISO data were freely downloaded from <http://marine.copernicus.eu>. We would like to thank more particularly Pierrette Duformontel (Ifremer, Toulon, France) and Christian Begler (GEOMAR, Kiel, Germany) for their precious help on glider CAMPE setup. N. K. wishes to thank Thomas Meunier for very constructive discussions on tracer stirring. AC wishes to thank the joint CNES/NASA OSTST project entitled "Merging of satellite and in situ observations for the analysis of meso and submesoscale dynamics". The authors are grateful toward both reviewers that contribute anonymously to greatly improve the manuscript. This work has been supported by the European Union's Horizon 2020 research and innovation program under grant agreements No 635359 (BRIDGES project) and No 633211 (AtlantOS project).

- Chaigneau, A., Gizolmea, A., & Gradosb, C. (2008). Mesoscale eddies off Peru in altimeter records: Identification algorithms and eddy spatio-temporal patterns. *Progress in Oceanography*, 79(2-4), 106–119. <https://doi.org/10.1016/j.pocean.2008.10.013>
- Chaigneau, A., Eldin, G., & Dewitte, B. (2009). Eddy activity in the four major upwelling systems from satellite altimetry (1992–2007). *Progress in Oceanography*, 83, 117–123. <https://doi.org/10.1016/j.pocean.2009.07.012f>
- Chelton, D. B., de Szoeke, R. A., & Schlax, M. G. (1998). Geographical variability of the first Rossby baroclinic radius of deformation. *Journal of Physical Oceanography*, 28(3), 433–460. [https://doi.org/10.1175/1520-0485\(1998\)028<0433:GVOTFB>2.0.CO;2](https://doi.org/10.1175/1520-0485(1998)028<0433:GVOTFB>2.0.CO;2)
- Chelton, D. B., Schlax, M. G., Samelson, R. M., & de Szoeke, R. A. (2007). Global observations of large oceanic eddies. *Geophysical Research Letters*, 34, L15606. <https://doi.org/10.1029/2007GL030812>
- Cole, S. T., & Rudnick, D. L. (2012). The spatial distribution and annual cycle of upper ocean thermohaline structure. *Journal of Geophysical Research*, 117, C02027. <https://doi.org/10.1029/2011JC007033>
- Cole, S. T., Rudnick, D. L., & Colosi, J. A. (2010). Seasonal evolution of upper-ocean horizontal structure and the remnant mixed layer. *Journal of Geophysical Research*, 115, C04012. <https://doi.org/10.1029/2009JC005654>
- du Plessis, M., Swart, S., Ansong, I. J., & Mahadevan, A. (2017). Submesoscale processes promote seasonal restratification in the Subantarctic Ocean. *Journal of Geophysical Research: Oceans*, 122, 2960–2975. <https://doi.org/10.1002/2016JC012494>
- Duteil, O., Schwarzkopf, F. U., Böning, C. W., & Oschlies, A. (2014). Major role of the equatorial current system in setting oxygen levels in the eastern tropical Atlantic Ocean: A high-resolution model study. *Geophysical Research Letters*, 41, 2033–2040. <https://doi.org/10.1002/2013GL058888>
- Emery, W. J., & Meincke, J. (1986). Global water masses: Summary and review. *Oceanologica Acta*, 9(4), 383–391.
- Ferrari, R., & Polzin, K. L. (2005). Fine scale structure of the T–S relation in the eastern North Atlantic. *Journal of Physical Oceanography*, 35, 1437–1454. <https://doi.org/10.1175/JPO2763.1>
- Fischer, T., Banyte, D., Brandt, P., Dengler, M., Krahnmann, G., Tanhua, T., & Visbeck, M. (2013). Diapycnal oxygen supply to the tropical North Atlantic oxygen minimum zone. *Biogeosciences*, 10, 5079–5093.
- Gaillard, F., Reynaud, T., Thierry, V., Kolodziejczyk, N., & von Schuckmann, K. (2016). *in situ*-based reanalysis of the global ocean temperature and salinity with ISAS: Variability of the heat content and steric height. *Journal of Climate*, 29(4), 1305–1323. <https://doi.org/10.1175/JCLI-D-15-0028.1>
- Garau, B., Ruiz, S., Zhang, W. G., Pascual, A., Heslop, E., Kerfoot, J., & Tintoré, J. (2011). Thermal lag correction on Slocum CTD glider data. *Journal of Atmospheric and Oceanic Technology*, 28, 1065–1071. <https://doi.org/10.1175/JTECH-D-10-05030.1>
- Gilbert, A. D. (1988). Spiral structures and spectra in two-dimensional turbulence. *Journal of Fluid Mechanics*, 193(1), 475–497. <https://doi.org/10.1017/S0022112088002228>
- Gouldn, J., & Coauthors (2004). Argo profiling floats bring new era of *in situ* ocean observations. *Eos, Transactions American Geophysical Union*, 85, 19. <https://doi.org/10.1029/2004EO190002>
- Hahn, J., Brandt, P., Greatbatch, R. J., Krahnmann, G., & Körtzinger, A. (2014). Oxygen variance and meridional oxygen supply in the Tropical North East Atlantic oxygen minimum zone. *Climate Dynamics*, 43(11), 2999–3024. <https://doi.org/10.1007/s00382-014-2065-0>
- Haynes, P., & Anglade, J. (1997). The vertical-scale cascade in the atmospheric tracers due to large-scale differential advection. *The Journal of the Atmospheric Sciences*, 54(9), 1121–1136. [https://doi.org/10.1175/1520-0469\(1997\)054<1121:TVSCIA>2.0.CO;2](https://doi.org/10.1175/1520-0469(1997)054<1121:TVSCIA>2.0.CO;2)
- Hua, B. L., Menesguen, C., Gentil, S. L., Schopp, R., Marsset, B., & Aiki, H. (2013). Layering and turbulence surrounding an anticyclonic oceanic vortex: *In situ* observations and quasi-geostrophic numerical simulations. *Journal of Fluid Mechanics*, 731, 418–442. <https://doi.org/10.1017/jfm.2013.369>
- Itoh, S., & Rudnick, D. L. (2017). Fine-scale variability of isopycnal salinity in the California Current System. *Journal of Geophysical Research: Oceans*, 122, 7066–7081. <https://doi.org/10.1002/2017JC013080>
- Jiang, H., Huang, R. X., & Wang, H. (2008). Role of gyration in the oceanic general circulation: Atlantic Ocean. *Journal of Geophysical Research*, 113, C03014. <https://doi.org/10.1029/2007JC004134>
- Karstensen, J., Fiedler, B., Schütte, F., Brandt, P., Körtzinger, A., Fisher, G., et al. (2015). Open ocean dead zone in the tropical North Atlantic Ocean. *Biogeosciences*, 12(1), 1–14. <https://doi.org/10.5194/bg-12-1-2015>
- Karstensen, J., Schütte, F., Pietri, A., Krahnmann, G., Fiedler, B., Grundle, D., et al. (2017). Upwelling and isolation in oxygen-depleted anticyclonic mode-water eddies and implications for nitrate cycling. *Biogeosciences*, 14(8), 2167–2181. <https://doi.org/10.5194/bg-14-2167-2017>
- Karstensen, J., Stramma, L., & Visbeck, M. (2008). Oxygen minimum zones in the eastern tropical Atlantic and Pacific oceans. *Progress in Oceanography*, 77(4), 331–350. <https://doi.org/10.1016/j.pocean.2007.05.009>
- Klein, P., Treguier, A.-M., & Hua, B. L. (1998). Three-dimensional stirring of the thermohaline front. *Journal of Marine Research*, 56(3), 589–612. <https://doi.org/10.1357/002224098765213595>
- Kolodziejczyk, N., Prigent-Mazella, A., & Fabienne, G. (2017). ISAS-15 temperature and salinity gridded fields. *SEANOE*. <https://doi.org/10.17882/52367>
- Laurent, S., & Schmitt, R. W. (1999). The contribution of salt fingers to vertical mixing in the North Atlantic tracer release experiment. *Journal of Physical Oceanography*, 29, 1404–1424. [https://doi.org/10.1175/1520-0485\(1999\)029<1404:TCOSFT>2.0.CO;2](https://doi.org/10.1175/1520-0485(1999)029<1404:TCOSFT>2.0.CO;2)
- Liblik, T., Karstensen, J., Testor, P., Alenius, P., Hayes, D., Ruiz, S., et al. (2016). Potential for an underwater glider component as part of the Global Ocean observing system. *Methods in Oceanography*, 17(50–82), 50–82. <https://doi.org/10.1016/j.mio.2016.05.001>
- Luyten, J. R., Pedlosky, J., & Stommel, H. (1983). The ventilated thermocline. *Journal of Physical Oceanography*, 13, 292–309. [https://doi.org/10.1175/1520-0485\(1983\)013<0292:TVT>2.0.CO;2](https://doi.org/10.1175/1520-0485(1983)013<0292:TVT>2.0.CO;2)
- Mahadevan, A., D'Asaro, E., Lee, C., & Perry, M. J. (2012). Eddy-driven stratification initiates North Atlantic spring phytoplankton blooms. *Science*, 337(6090), 54–58. <https://doi.org/10.1126/science.1218740>
- May, D. G., & Kelley, D. E. (1997). Effect of baroclinicity on double-diffusive interleaving. *Journal of Physical Oceanography*, 27(9), 1997–2008. [https://doi.org/10.1175/1520-0485\(1997\)027<1997:EOBODD>2.0.CO;2](https://doi.org/10.1175/1520-0485(1997)027<1997:EOBODD>2.0.CO;2)
- McDougall, T. J., & Ruddick, B. R. (1992). The use of ocean to quantify both turbulent mixing and salt-fingering. *Deep Sea Research*, 39, 1931–1952.
- Meunier, T., Menesguen, C., Schopp, R., & Gentil, S. L. (2015). Tracer stirring around a meddy: The formation of layering. *Journal of Physical Oceanography*, 45(2), 407–423. <https://doi.org/10.1175/JPO-D-14-0061.1>
- Ndoye, X., Capet, P., Estrade, B., Sow, D., Dagorne, A., Lazar, A., & Gaye, P. B. (2014). SST patterns and dynamics of the Southern Senegal-Gambia upwelling center. *Journal of Geophysical Research: Oceans*, 119, 8315–8335. <https://doi.org/10.1002/2014JC010242>
- Pegliasco, C., Chaigneau, A., & Morrow, R. (2015). Main eddy vertical structures observed in the four major Eastern Boundary Upwelling Systems. *Journal of Geophysical Research: Oceans*, 120, 6008–6033. <https://doi.org/10.1002/2015JC010950>
- Pietri, A., & Karstensen, J. (2018). Dynamical characterization of a low oxygen submesoscale coherent vortex in the eastern North Atlantic Ocean. *Journal of Geophysical Research: Oceans*, 123, 2049–2065. <https://doi.org/10.1002/2017JC013177>

- Pietri, A., Testor, P., Echevin, V., Chaigneau, A., Mortier, L., Eldin, G., & Grados, C. (2013). Finescale vertical structure of the upwelling system off southern Peru as observed from glider data. *Journal of Physical Oceanography*, 43(3), 631–646. <https://doi.org/10.1175/JPO-D-12-035.1>
- Ruddick, B. (1992). Intrusive mixing in Mediterranean salt lens—Intrusion slope and dynamical mechanisms. *Journal of Physical Oceanography*, 22(11), 1274–1285. [https://doi.org/10.1175/1520-0485\(1992\)022<1274:MIAMS>2.0.CO;2](https://doi.org/10.1175/1520-0485(1992)022<1274:MIAMS>2.0.CO;2)
- Rudnick, D., Davis, L. R. E., Eriksen, C. C., Fratantoni, D. M., & Perry, M. J. (2004). Underwater gliders for ocean research. *Marketing Technological Journal*, 38, 48–59.
- Rudnick, D. L., & Martin, J. P. (2002). On the horizontal density ratio in the upper ocean. *Dynamics of Atmospheres and Oceans*, 36, 3–21.
- Schott, F. A., Fischer, J., & Stramma, L. (1998). Transports and pathways of the upper-layer circulation in the western tropical Atlantic. *Journal of Physical Oceanography*, 28(10), 1904–1928. [https://doi.org/10.1175/15200485\(1998\)028<1904:TAPOTU>2.0.CO;2](https://doi.org/10.1175/15200485(1998)028<1904:TAPOTU>2.0.CO;2)
- Schott, F. A., Stramma, L., & Fischer, J. (1995). The warm water inflow into the western tropical Atlantic boundary regime, spring 1994. *Journal of Geophysical Research*, 100(C12), 24,745–24,760. <https://doi.org/10.1029/95JC02803>
- Schütte, F., Brandt, P., & Karstensen, J. (2016). Occurrence and characteristics of mesoscale eddies in the tropical northeast Atlantic Ocean. *Ocean Science*, 12, 663–685. <https://doi.org/10.5194/os-12-663-2016a>
- Schütte, F., Karstensen, J., Krahmann, G., Hauss, H., Fiedler, B., Brandt, P., et al. (2016). Characterization of “dead-zone” eddies in the Eastern tropical North Atlantic. *Biogeosciences*, 13(20), 5865–5881. <https://doi.org/10.5194/bg-13-5865-2016>
- Siedler, G., Zangenberg, N., Onken, R., & Morlière, A. (1992). Seasonal changes in the tropical Atlantic circulation: Observation and simulation of the Guinea Dome. *Journal of Geophysical Research*, 97(C1), 703–715. <https://doi.org/10.1029/91JC02501>
- Smith, K. S., & Ferrari, R. (2009). The production and dissipation of compensated thermohaline variance by mesoscale stirring. *Journal of Physical Oceanography*, 39(10), 2477–2501. <https://doi.org/10.1175/2009JPO4103.1>
- Stramma, L., Brandt, P., Schafstall, J., Schott, F., Fischer, J., & Körtzinger, A. (2008). Oxygen minimum zone in the North Atlantic south and east of the Cape Verde Islands. *Journal of Geophysical Research*, 113, C04014. <https://doi.org/10.1029/2007JC004369>
- Takeshita, Y., Martz, T. R., Johnson, K. S., Plant, J. N., Gilbert, D., Riser, S. C., et al. (2013). A climatology-based quality control procedure for profiling float oxygen data. *Journal of Geophysical Research: Oceans*, 118, 5640–5650. <https://doi.org/10.1002/jgrc.20399>
- Testor, P., and Coauthors, (2010). Gliders as a component of future observing systems. Proc. OceanObs09: Sustained Ocean Observations and Information for Society, Vol. 2, Venice, Italy, ESA, WPP-306. Retrieved from <http://www.oceanobs09.net/proceedings/cwp/cwp89/>
- Thierry, V., Bittig, H., Gilbert, D., Kobayashi, T., Sato, K., & Schmid, C. (2016). *Processing Argo OXYGEN data at the DAC level, v2.2*. <https://doi.org/10.13155/39795>
- Thompson, A., Lazar, A., Buckingham, C., Naveira Garabato, A. C., Damerell, G. M., & Heywood, K. J. (2016). Open-ocean submesoscale motions: A full seasonal cycle of mixed layer instabilities from gliders. *Journal of Physical Oceanography*, 46(4), 1285–1307. <https://doi.org/10.1175/JPO-D-15-0170.1>
- Thomsen, S., Kanzow, T., Colas, F., Echevin, V., Krahmann, G., & Engel, A. (2016). Do submesoscale frontal processes ventilate the oxygen minimum zone off Peru? *Geophysical Research Letters*, 43, 8133–8142. <https://doi.org/10.1002/2016GL070548>
- Tsuchiya, M., Talley, L. D., & McCartney, M. S. (1992). An eastern Atlantic section from Iceland southward across the equator. *Deep-Sea Research Part I*, 39(11–12), 1885–1917. [https://doi.org/10.1016/0198-0149\(92\)90004-D](https://doi.org/10.1016/0198-0149(92)90004-D)
- Wyrtki, K. (1962). The oxygen minima in relation to ocean circulation. *Deep Sea Research*, 9, 11–23.
- Yamagata, T., & Iisuka, S. (1995). Simulation of the Tropical Thermal Domes in the Atlantic: A seasonal cycle. *Journal of Physical Oceanography*, 15, 2129–2140.
- You, Y. (2002). A global ocean climatological atlas of the Turner angle: Implications for double-diffusion and water-mass structure. *Deep Sea Research, Part I*, 49(11), 2075–2093. [https://doi.org/10.1016/S0967-0637\(02\)00099-7](https://doi.org/10.1016/S0967-0637(02)00099-7)
- Zenk, W., Klein, B., & Schroder, M. (1991). Cape Verde frontal zone. *Deep Sea Research Part A Oceanographic Research Papers*, 38, S505–S530. [https://doi.org/10.1016/S0198-0149\(12\)80022-7](https://doi.org/10.1016/S0198-0149(12)80022-7)